Materials & Design 217 (2022) 110640

Contents lists available at ScienceDirect

Materials & Design

journal homepage: www.elsevier.com/locate/matdes

Experimental and modeling investigations of the non-isothermal and isothermal precipitations in an Al-Cu-Mg-Zr alloy with various pre-precipitation microstructures

Guowei Bo [a,b], Yinlu Wang [a], Mingcai Liu [a], Jie Tang [a,*], Fulin Jiang [a,*], Jie Teng [a], Gang Xiao [a,c], Dingfa Fu [a], Hui Zhang [a,*]

[a] College of Materials Science and Engineering, Hunan University, Changsha 410082, China
[b] Chair of Materials Engineering of Additive Manufacturing, TUM School of Engineering and Design, Technical University of Munich, Boltzmannstr. 15, Garching bei Munich, 85748, Germany
[c] JIANGXI KMAX Industrial Co., Ltd., Nanchang 330100, China

HIGHLIGHTS

- Precipitation behaviors of Al-Cu-Mg-Zr alloy were highly dependent on pre-precipitation microstructures and thermal history.
- A temperature–time-microstructure-properties map was established to unravel precipitation characteristics and their strengthening functions.
- The *in situ* electrical resistivity was used as the main input data to develop an improved model based on the classical Kampmann and Wagner type numerical model.
- The maximum hardness for heat-treated alloys is mainly attributed to the co-existence of Guinier-Preston-Bagaryatsky (GPB) zones and *S* phase.

GRAPHICAL ABSTRACT

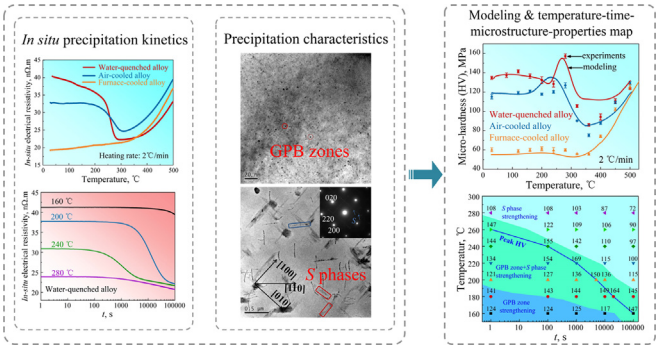

ARTICLE INFO

Article history:
Received 1 December 2021
Revised 18 March 2022
Accepted 6 April 2022
Available online 11 April 2022

Keywords:
Al-Cu-Mg alloy
Precipitation
Heat treatment
In situ electrical resistivity
Strengthening

ABSTRACT

The complex precipitation evolutions of Al-Cu-Mg alloys during both non-isothermal and isothermal thermal processes have been found to work on their mechanical properties and electrical resistivity. Modeling of the precipitation kinetics, electrical resistivity and strength evolution is therefore essential for optimizing heat treatment and processing of these alloys. In this work, *in situ* electrical resistivity monitoring during both non-isothermal and isothermal thermal processes and microstructural characterizations were conducted on an Al-Cu-Mg-Zr alloy with different pre-precipitation microstructures to provide fundamental insights of precipitation behaviors. The results showed that precipitation behaviors of Al-Cu-Mg-Zr alloy, such as the dominant strengthening phase, were highly dependent on pre-precipitation microstructures and thermal history. A time–temperature-microstructure-properties map was established to unravel precipitation characteristics and their strengthening functions. The maximum hardness was indicated to be attributed to the combined presence of Guinier–Preston–Bagaryatsky (GPB) zones and fine *S* (Al_2CuMg) phase. Further, *in situ* electrical resistivity was used as the main input data to

* Corresponding authors.
E-mail addresses: tangj94@hnu.edu.cn (J. Tang), jfling2820@163.com (F. Jiang), zhanghui63hunu@163.com, zhanghui63@hnu.edu.cn (H. Zhang).

https://doi.org/10.1016/j.matdes.2022.110640

develop an improved model based on the classical Kampmann and Wagner type numerical model (KWN model). This integrated model could not only reveal precipitation kinetics but also well predict hardness evolutions of the studied alloy during non-isothermal and isothermal processes.

1. Introduction

Al-Cu-Mg alloys are widely used as structural components in automotive and aviation industry due to their low cost and low density to strength ratio [1]. The high strength of these alloys is dominantly attributed to a series of fine precipitates, such as Guinier-Preston-Bagaryatsky (GPB) zones, *S* (Al_2CuMg) and θ (Al_2Cu) phases [1-3], and the type of major strengtheners are highly dependent on the Cu:Mg ratio in Al-Cu-Mg alloys [4-8]. Over the decades, a number of studies have been published on the composition and crystal structure of such precipitates [5-15]. Generally, GPB zones were early thought to be rod-like particles with size of 1–2 nm in diameter and 4–8 nm in length, and to have tetragonal lattice with parameters a = 0.55 nm, c = 0.404 nm. Further, it was recently proposed that the GPB zones encompassed a variety of compositions and atomic structures, such as one-dimensional (1D) units GPB1/GPB1* [10] and composite GPB/GPBII zones [11]. With regard to *S* phase, it was definite that its stable structure was a ternary Al_2CuMg compound with orthorhombic crystal structure (a = 0.400 nm, b = 0.923 nm, c = 0.714 nm), predominantly forming with a lath/rod-like morphology [4-11]. Several intermediate structures of *S* phase were also proposed, such as *S″* and *S′* phases. The crystallographic structures of *S″* and *S′* phases were considered to be identical to *S* phase, but *S″* phase was understood as a phase highly coherent with Al matrix, and *S′* phase as a strained version of *S* phase [7].

Meanwhile, particular attention was paid to the precipitation sequence of Al-Cu-Mg alloys. By utilizing atom probe technology [4,5,16,17], the atomic clusters were considered as the first precipitated microstructure instead of the ranking of GPB zones. The clusters were distinguished from GPB zones due to the lack of characteristic shape, composition and crystal structure, while GPB is generally considered to be a short range ordering of Cu and Mg solute atoms [4-7]. On the other hand, it is widely accepted that the formation of stable *S* phase is preceded by the appearance of Cu-Mg co-clusters, GPB zones as well as different metastable precursors like *S″* phase and *S′* phase [4-8,18,19]. However, little study could reliably reveal the existence of *S″* phase. Moreover, two types of stable *S* phase were also reported to be able to form as a function of Si content and work hardening [8,9,20-22]. Hence, the exact precipitation sequence for Al-Cu-Mg alloys depends on alloy composition and ageing conditions, and is still under debate. It is generally written as below [4-10]:

SSS (supersaturated solid solution)→ Cu-Mg clusters → GPB zone → *S′*→ *S* (Type I)→ *S* (Type II).

Further, the precipitation hardening in Al-Cu-Mg alloys is widely thought to be a two-stage process [7,23]. The first stage may account for as much as 70% of total hardening and may be complete after ageing for only 60 s [5,7,24]. Earlier X-ray diffraction studies concluded that the first stage of hardening was associated with the formation of GPB zones [13]. However, Reich et al. [17] did not detect the presence of GPB zones during the first hardening stage of ageing by several advanced microscopies. Later works showed that the rapid formation of Cu-Mg co-clusters, which formed within minutes after solid solution treatment, was responsible for this initial age hardening [7,25-27]. As to the second hardening stage, early works showed that it was mainly accompanied the formation of thermodynamic equilibrium *S* phase [7,8]. Some works also found that heterogeneous nucleation of *S* phase or metastable *S′* phase occurred on dislocation lines in the early ageing process [28,29]. Recently, the second stage of hardening was attributed to the combined presence of these GPB zones, *S′* phase and/or *S* phase [4,5].

In general, most efforts of the published works were mainly put into the qualitative characteristic of precipitates under isothermal artificial ageing [2-6,27-30]. The hardness evolution curves combined with transmission electron microscopy (TEM) characterization were the main approaches in these works, so the results were time consuming, *ex situ* and discontinuous, which might result in large specimen to specimen variations. Nevertheless, complicated thermal conditions were generally involved during heating ramp (non-isothermal), preheating (isothermal) and interval holding of multistep industrial hot working of Al-Cu-Mg alloys, and it has been found that pre-precipitation microstructures had considerable influences on dynamic and static precipitation as well as hot workability of Al-Cu-Mg alloys [31,32]. Therefore, the precipitation evolutions under various thermal histories still need more studies.

In addition, to gain a better understanding of the nature and strengthening contribution of precipitates, many investigations [33-40] were conducted on the modeling of precipitation evolutions in Al alloys (especially in Al-Mg-Si alloys), such as the volume fraction and size of precipitates during ageing. In these works, two main approaches were employed. In one of the approaches, the modeling of nucleation, growth and impingement of precipitates were based on the concepts of the Johnson–Mehl–Avrami-Kolmogorov (JMAK) model and the modeling of coarsening kinetics was based on the Liftshitz-Slyozov-Wagner (LSW) theory. In another approach, the Kampmann and Wagner type numerical model (KWN model) [41] was used to predict the complete precipitation kinetics from nucleation to coarsening stages. In addition, the modeling of precipitation strengthening was mainly based on the interaction of precipitates (both shearable and non-shearable) with dislocations [38]. For Al-Cu-Mg alloys, Khan et al. [39,40] obtained a good prediction of the volume fraction, size and strengthening contribution of *S* phase during isothermal and non-isothermal treatments using the KWN model. However, the models in most published works were mainly about the strengthening contribution from single precipitation phase, and some model parameters were not given or based on the statistic results of microstructural characterizations in which the error was inevitable. Therefore, more attention should be paid to the quantitative evaluation of precipitation evolution and the related modeling of Al-Cu-Mg alloys aged under a wide range of isothermal and non-isothermal conditions.

In this work, an optimized Al-Cu-Mg-Zr alloy, which was designed to improve the mechanical properties of 2024 Al alloy by increasing the addition of Zr and lowering the impurities [42], was used to unravel its complex precipitation behavior during non-thermal and isothermal heat treatment processes. Because electrical resistivity has been confirmed to be a very effective and reliable approach to monitor the formation and dissolution of precipitates during the heat treatment processes in various metallic materials (e.g., aluminum alloy and magnesium alloy) [43-46], the *in situ* electrical resistivity monitoring combined with micro-hardness test and TEM observation were employed to inves-

tigate precipitation kinetics and microstructure evolution of the studied alloy. Then the precipitation thermodynamics and kinetics were revealed and the strength evolutions were well predicted by developing an integrated model in which the *in situ* electrical resistivity results were the main input data. Further, because Al-Cu-Mg alloys were commonly subject to different heat treatment patterns prior to industrial hot working operation which resulted in various precipitation microstructures, three groups of Al-Cu-Mg-Zr alloy specimens with different pre-precipitation microstructures were tailored through air cooling (AC), water quenching (WQ) and furnace cooling (FC) after solution heat treatment to obtain the in-depth understanding of the effects of different pre-precipitation microstructures on precipitation evolutions.

2. Materials and methods

The as-received Al-Cu-Mg-Zr alloy with Cu:Mg atomic ratio close to 1 was adopted in this study. The detailed chemical composition is given in Table 1. Three cooling conditions were employed for the hot-rolled alloy after solution heat treatment (500 °C/2h). The specimens undergoing air cooling are denoted as AC alloy; the samples quenched in water are denoted as WQ alloy, and the specimens cooled in furnace are denoted as FC alloy. Then, each group specimen was machined into thin pieces with the size of 50 mm × 5 mm × 1 mm for *in situ* electrical resistivity measurement which employed the four-point probe method, as illustrated in previous work [43]. For non-isothermal *in situ* electrical resistivity tests, two heating rates (i.e., 2 °C/min and 10 °C/min) were adopted to heat the specimen from room temperature to 500 °C. The isothermal *in situ* electrical resistivity tests were carried out at different temperatures (i.e., 160 °C, 200 °C, 240 °C, 280 °C) for 100000 s. Before isothermal holding stage, the specimens were heated to the target temperatures with the furnace, which is closer to industrial practical applications. In addition, selected specimens quenched at different temperature and/or holding time during non-isothermal and isothermal treatment were also examined by micro-hardness measurements, scanning electron microscopy (SEM) and TEM to investigate the precipitation behaviors of the studied alloy. For micro-hardness tests, five hardness examinations were made on each polished sample and the average values were used. The specimens for TEM characterization specimens were prepared using common methods [32,33]. Digital bright field images taken near the $[001]_{Al}$ zone axis were analyzed manually using the dimension feature in Image-Pro Plus software to manually estimate precipitates size.

3. Experimental results

3.1. Pre-precipitation microstructures

Fig. 1 presents the SEM and TEM micrographs of the prepared specimens with different pre-precipitation microstructures for subsequent non-isothermal and isothermal heat treatment processes. As shown in SEM images, there are coarse constituent phases along grain boundaries in all specimens. Numerous fine precipitates inside grains are exhibited in AC alloy (Fig. 1(a)). In WQ alloy (Fig. 1(b)), little precipitates are observed in grain interiors. Many coarse precipitates are also formed in grain interiors of FC alloy, because the very slow cooling rate could provide enough time for the growth and coarsening of precipitates (Fig. 1(c)). The fractions of particle area for AC, WQ and FC alloy are quantitatively estimated to be approximate 8.89%, 1.99% and 14.17%, respectively. In addition, the precipitates inside grains are also observed under TEM, as shown in Fig. 1 (d)-(f). The difference in pre-precipitation microstructures among three groups of specimens is similar with that observed under SEM. In the tables at the top right of Fig. 1(d) and (f), the Energy Dispersive Spectrometer (EDS) analysis of the precipitates marked as A and B indicate the presence of θ (Al_2Cu) phases, which should be formed between 350 ~ 450 °C during cooling process according to the calculated equilibrium phase fraction diagram of the present Al-Cu-Mg-Zr alloy in Fig. 2. In addition, a very large precipitate is also observed in FC alloy, as shown in Fig. 1(f). By contrast, in WQ alloy, there are little precipitates in WQ alloy because of solution treatment, while lots of dislocations due to rapid cooling rate.

3.2. In situ electrical resistivity and micro-hardness evolutions during non-isothermal and isothermal processes

Fig. 3 (a) shows the *in situ* electrical resistivity ($\Delta\rho$) evolutions of Al-Cu-Mg-Zr alloy specimens with various pre-precipitation microstructures during non-isothermal processes (continuous heating). The value of temperature independent $\Delta\rho$ was obtained based on the following equation:

$$\Delta\rho = \rho(T) - \rho_{Al}(T) \quad (1)$$

where $\rho(T)$ was the timely measured electrical resistivity of Al-Cu-Mg-Zr alloy at particular temperature (T), and $\rho_{Al}(T)$ was the electrical resistivity of pure Al at given temperature (T): $\rho_{Al}(T)$ = 23.9762 + 0.1242 T (nΩ·m) [44-46]. According to the Matthiessen's rule, $\Delta\rho$ is dominantly the function of residual impurity (i.e., supersaturated solid solution) when plastic strain (or dislocation) is absent [44-46]. As a result, $\Delta\rho$ decreases gradually with the decomposition of supersaturated solid solution during precipitation process. When precipitates are re-dissolved, $\Delta\rho$ will increase. In Fig. 3 (a), clear influences of different pre-precipitation microstructures on $\Delta\rho$ evolution are indicated. Overall, $\Delta\rho$ of WQ alloy presents a slight decreasing stage and then a rapid drop, followed by an increasing stage. Compared with WQ alloy, $\Delta\rho$ of AC alloy shows a similar trend after the initial constant stage at lower temperatures. By contrast, $\Delta\rho$ of FC alloy first indicates a slight increasing stage in lower temperature range, and then increases rapidly over ~ 360 °C.

Further, as shown in Fig. 3 (b), the differentiation of $\Delta\rho$ with respect to temperature ($d\Delta\rho/dT$) could provide a more detailed indication of decreasing and increasing rate, which could indicate precipitate formation and dissolution rate. When heated at 2 °C/min, the slight increase of $d\Delta\rho/dT$ in WQ alloy at the low temperature range (<240 °C) indicates slow formation of precipitates. Above ~ 240 °C, the fast precipitation leads to rapid increase in $d\Delta\rho/dT$ of WQ alloy. The $d\Delta\rho/dT$ of WQ alloy at approximate 280 °C is nearly equal to zero, indicating the minimum $\Delta\rho$. When the temperature is between 280 °C and 360 °C, the $d\Delta\rho/dT$ of WQ alloy is higher than zero but owns a much low value, indicating that the increasing temperature results in the very slight increase of $\Delta\rho$. Subsequently, the higher $d\Delta\rho/dT$ in the temperature range

Table 1
Chemical composition of the studied alloy.

Element	Cu	Mg	Mn	Zr	Si	Fe	Al
wt. %	4.10	1.42	0.57	0.12	<0.05	<0.07	Bal.
at. %	1.7	1.6	0.28	0.03	<0.05	<0.03	Bal.

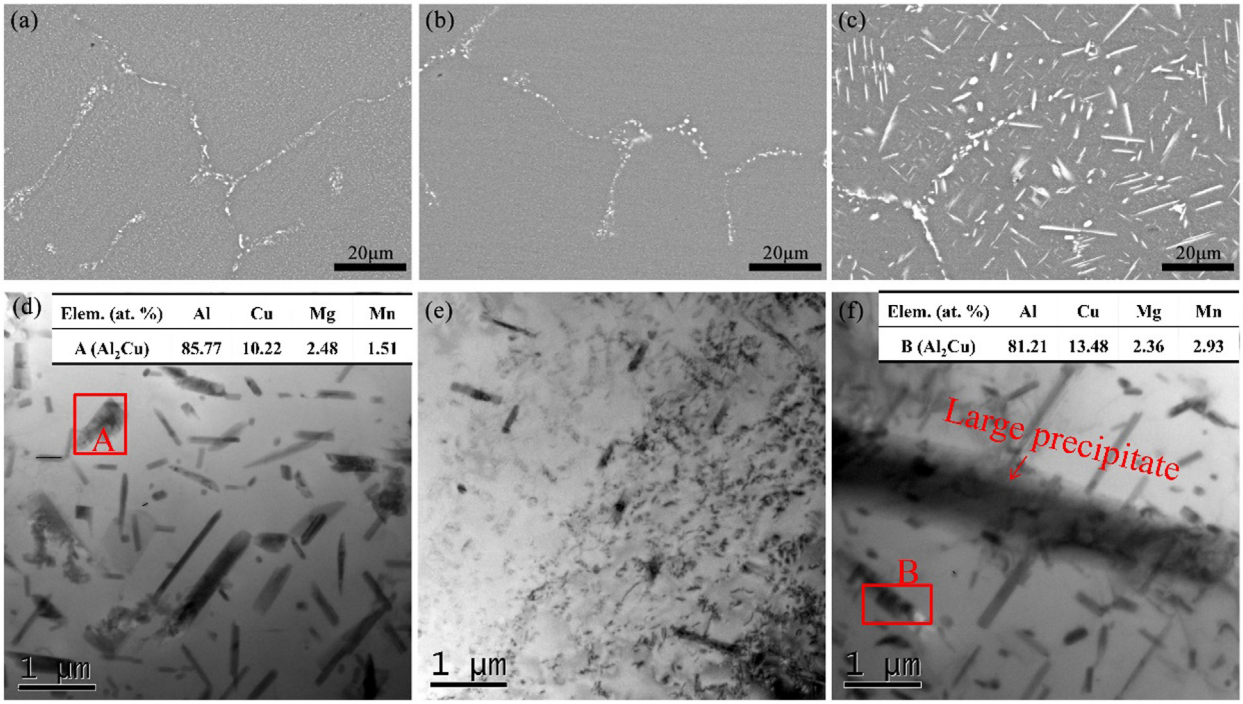

Fig. 1. SEM and TEM micrographs of the studied alloy specimens: (a) & (d) AC alloy; (b) & (e) WQ alloy; (c) & (f) FC alloy.

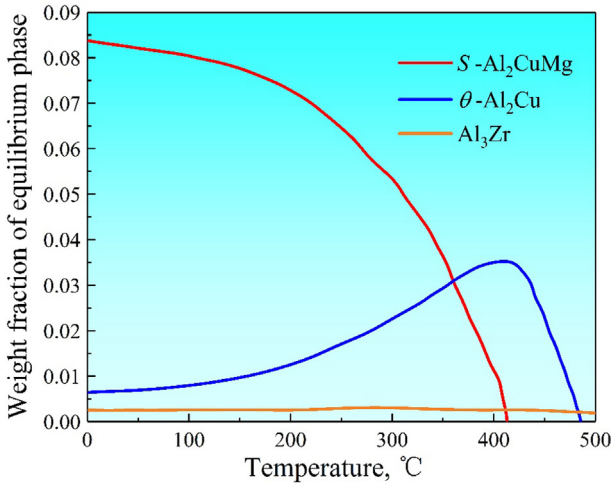

Fig. 2. The calculated equilibrium phase fraction diagram of the present Al-Cu-Mg-Zr alloy using Thermo-Calc software [32].

of 360 °C to 500 °C shows an increase of $\Delta\rho$ owing to the fast re-dissolution of precipitates. For AC alloy heated at 2 °C/min, $d\Delta\rho/dT$ is close to zero under 200 °C, indicating few formation and/or dissolution of precipitates during this stage. After that, the negative values of $d\Delta\rho/dT$ between 200 °C and 300 °C indicate the beginning of precipitates formation, and the formation rate increases first and then decreases. Moreover, it is clear that the $d\Delta\rho/dT$ magnitude of AC alloy, especially the minimum $d\Delta\rho/dT$ representing the maximum formation rate, is lower than that of WQ alloy during precipitation stage, indicating that precipitates form more quickly in WQ alloy than AC alloy. However, the temperature for $d\Delta\rho/dT$ of AC alloy nearly equal to zero is approximate 300 °C, indicating the later dissolution of AC alloy than WQ alloy during heating process. In temperature range from 300 °C to 500 °C, the increasing $d\Delta\rho/dT$ with positive value for AC alloy is always higher that for WQ alloy, indicating the occurrence of faster dissolution of precipitates in AC alloy. For FC alloy, the dissolution of precipitates occurred during the whole heating process, especially in higher temperature range, because $d\Delta\rho/dT$ is always positive value and increases with temperature. In addition, the heating rate is also observed to influence the evolution of $\Delta\rho$. At the higher heating rate of 10 °C/min, the evolution trends of $\Delta\rho$ are almost identical to that of 2 °C/min for the three alloy tempers. However, the transition temperatures of precipitation formation and dissolution are higher and the drop of $\Delta\rho$ is less at 10 °C/min than that at 2 °C/min. This is because under a higher heating rate, less time is left for the formation of precipitates during continuous heating. Hence, the monitored $\Delta\rho$ timely reveals the different precipitation behaviors of Al-Cu-Mg-Zr alloy under various heating rates.

The micro-hardness evolutions of Al-Cu-Mg-Zr alloy specimens quenched at various temperatures during continuous heating processes are shown in Fig. 3 (c) and (d). For WQ specimens with a heating rate of 2 °C/min, there is a slight increase in micro-hardness below 120 °C and then a decreasing stage below 240 °C, after which a rapid increase to peak value is observed at approximate 280 °C. Then the micro-hardness of WQ alloy decreases to a minimum at 360 °C followed by continuous increasing trend again. Compared with WQ alloy, the micro-hardness of AC alloy heated at 2 °C/min shows a similar trend in addition to the initial roughly unchanged stage below 240 °C. By contrast, the micro-hardness of FC alloy with a heating rate of 2 °C/min keeps almost constant below 360 °C, followed by continuous increasing stage. In addition to that the temperatures of transitions to the maximum and minimum hardness turn higher, similar evolutions of micro-hardness are observed for WQ and FC alloys with a higher heating rate of 10 °C/min (Fig. 3 (d)). However, the peak value of micro-hardness for AC alloy is obtained at a lower temperature (240 °C). By comparing to the *in situ* electrical resistivity results in Fig. 3 (a), it is clearly revealed that the peak hardness corresponds to the minimum value of $\Delta\rho$. When slight change of $\Delta\rho$ is indicated in Fig. 3 (a), hardness also varies slightly in Fig. 3 (c). Therefore, the increased hardness should mainly attribute to the

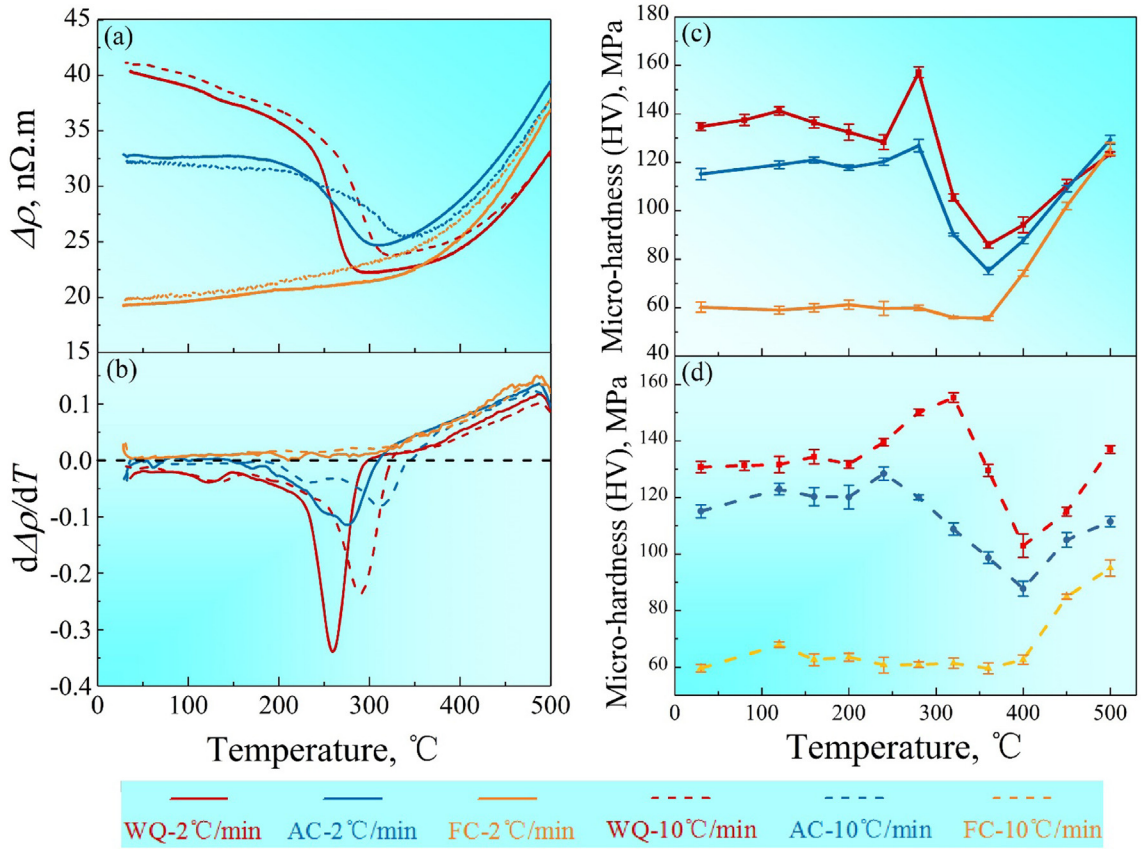

Fig. 3. (a) *In situ* electrical resistivity, (b) $d\Delta\rho/dT$, (c) and (d) micro-hardness evolutions of Al-Cu-Mg-Zr alloy during non-isothermal processes (continuous heating).

formation of numerous precipitates during non-isothermal heat treatments, which will be identified by subsequent microstructural observations.

Fig. 4 (a)-(c) present the evolutions of $\Delta\rho$ with holding time (t) during different isothermal treatments in the temperature range of 160–280 °C for all Al-Cu-Mg-Zr alloy tempers. In Fig. 3, it was shown that higher holding temperature would result in more precipitation during pre-heating processes. Consequently, the initial values of $\Delta\rho$ at the beginning of holding stage generally decrease with increasing holding temperature for all specimens. At the initial stage of isothermal holding, $\Delta\rho$ of all alloy specimens exhibits a constant stage, in which the durations drop with the increasing holding temperature. After that, $\Delta\rho$ decreases gradually with holding time. For instance, when the WQ alloy sample is held at 160 °C,

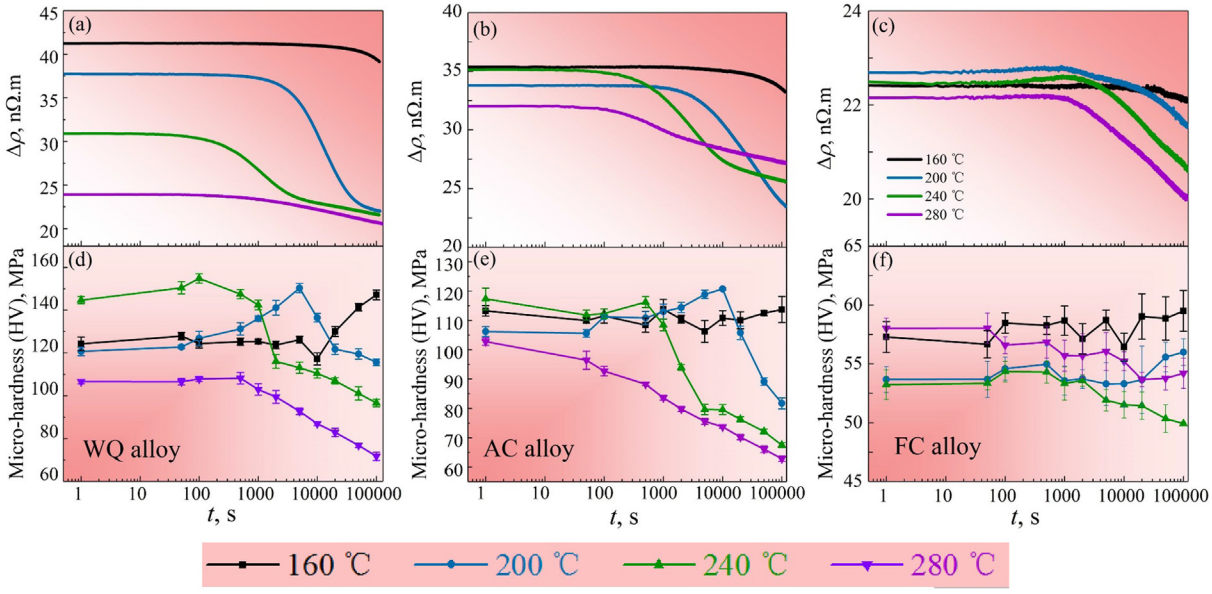

Fig. 4. (a)-(c) *In situ* electrical resistivity and (d)-(f) micro-hardness evolutions of Al-Cu-Mg-Zr alloy during isothermal holding processes.

$\Delta\rho$ presents a long stable period approximate 17000 s before slight decrease of $\Delta\rho$ is observed. The duration of constant stage at 200 °C, 240 °C and 280 °C for WQ alloy specimen is approximate 1000 s, 100 s and 50 s, respectively. The drop of electrical resistivity gradually slows down at the end of isothermal holding. More importantly, clear influences of different pre-precipitation microstructures are also indicated. For example, increased holding temperature leads to a decrease in $\Delta\rho$ value at 10^5 s for WQ and FC alloys, but that for AC alloy decreases first and then increases. In addition, the magnitudes of the drop in $\Delta\rho$ at 10^5 s for WQ and AC alloys are much higher than that for FC alloy at the same holding temperature. However, at 280 °C, the magnitude of the drop in $\Delta\rho$ at 10^5 s for WQ alloy is lower than AC alloy, indicating that more precipitates form in AC alloy. For all alloy tempers, WQ alloy owns the maximum $\Delta\rho$ of 41 nΩ·m, and the minimum value of $\Delta\rho$ in all experiments is about 20 nΩ·m.

Fig. 4 (d)-(f) show the micro-hardness evolutions with holding time (t) during different isothermal treatments in the temperature range of 160–280 °C for all alloy tempers, which are closely related to the precipitation behaviors as indicated by *in situ* electrical resistivity (Fig. 4(a)-(c)). Clear influences from pre-precipitation microstructures and holding temperature are indicated. For WQ alloy, steady stage is observed in the initial holding stage under all temperatures, in which the durations decrease with increasing holding temperature. After that, micro-hardness starts to increase and/or then decrease. The time to reach peak hardness decreases with rising holding temperature. When held at 160 °C, for instance, continuous increment of hardness is revealed after about 10^4 s and then it turns to peak value of 147 MPa till the end of holding (10^5 s). The peak hardness values are presented at 5000 s and 100 s for specimens annealed at 200 °C and 240 °C, respectively. However, there is little evident peak hardness for specimens annealed at 280 °C, indicating that the peak hardness has been obtained during pre-heating process. For AC alloy, the hardness keeps roughly unchanged at 160 °C. When held at 200 °C and 240 °C, the hardness evolution of AC alloy is similar to that of WQ alloy, but the time to reach peak hardness becomes longer (10^4 s for 200 °C and 1000 s for 240 °C) and the values of peak hardness are much smaller than those of WQ alloy. With holding temperature increasing to 280 °C, a continuous drop of hardness for AC alloy is indicated. By contrast, slight variation and minor decrease on hardness are observed for FC specimens holding at lower temperature (160 °C and 200 °C) and higher temperature (240 °C and 280 °C), respectively.

3.3. TEM observation of precipitation characteristics during non-isothermal and isothermal processes

Fig. 5 illustrates the TEM micrographs of selected WQ specimens quenched at different temperatures during continuous heating process (2 °C /min). As shown in Fig. 5 (a), dense GPB zones and few sparse constituent phases are observed in WQ specimen when heated to 200 °C. In Fig. 5 (b), weak spots from GPB zones in selected area electron diffraction (SAED) patterns are also indicated [9-12]. With temperature increasing to 280 °C, GPB zones become coarser (Fig. 5 (c)), and clear and strong spots in SAED patterns indicating the formation of numerous *S* phases are observed (Fig. 5 (d)) [6-8]. Then, a further increase to 360 °C in temperature results in complete dissolution of GPB zones and growth and/or coarsening of *S* phases, as shown in Fig. 5 (e) and (f). With temperature rising from 360 °C to 500 °C, coarser *S* phases also dissolve gradually, so there is almost no precipitates in specimens quenched at 500 °C, except few sparse coarse and irregular constituent precipitates (Fig. 5 (g) and (h)).

TEM characterizations of selected AC specimens quenched at different temperature are also employed to reveal the precipitation behaviors during continuous heating process (2 °C /min), as shown in Fig. 6. Compared with WQ alloy, little GPB zones are observed and a certain amount of *S* phases accompanied with a few blocky θ phases are observed in the AC specimens heated to 200 °C (Fig. 6 (a) and (b)). When temperature rose from 200 °C to 280 °C, GPB zones form gradually, and the precipitation of new *S* phases or coarsening of the pre-existing *S* phases are indicated (Fig. 6 (c) and (d)). With temperature increasing to 360 °C, complete dissolution of GPB zones and more *S* phases are observed (Fig. 6 (e) and (f)). But the coarsening of *S* phases is not evident compared with that in WQ alloy. After heating to 500 °C, the dissolution of *S* phase leads to little fine precipitates, but some coarse constituent phases are still presented (Fig. 6 (g) and (h)).

During isothermal holding at the given temperature (160 °C-280 °C), the precipitation evolution of the studied alloy mainly involves the formation and coarsening processes of precipitates, and the dissolution of *S* phase is almost absent. Therefore, the precipitation evolutions during isothermal processes are mainly dependent on holding time. For this sake, TEM characterizations are only employed in WQ alloy specimens to study the precipitation behavior of the present Al-Cu-Mg-Zr alloy during isothermal processes. Fig. 7 shows the TEM images of selected WQ samples under different isothermal conditions. As shown in Fig. 7 (a)-(d), (g) and (h), fine and dense GPB zones and *S* phases coexist evenly in these WQ specimens held at 160 °C for 10^5 s, 180 °C for 20000 s and 200 °C for 5000 s. On the other hand, it is well known that during isothermal processes the phase transformations and associated evolution of mechanical properties in Al-Cu-Mg alloys for different aging treatment (including high aging temperatures and longer durations) are very important references for practical situations. Therefore, a temperature–time-microstructure-properties map (TTMP) is obtained based on previous micro-hardness and precipitation characteristics results, as shown in Fig. 8. One can see that the time to reach peak micro-hardness decreases with increasing temperature. Meanwhile, all maximum micro-hardness are observed in the specimens with coexistence of GPB zones and *S* phases (Fig. 7 (a)-(d), (g) and (h)). By contrast, GPB zones dissolve and *S* phases coarsen when the holding time of the sample held at 180 °C increases to 10^5 s (Fig. 7 (e) and (f)), leading to a significant decrease in micro-hardness. In addition, the WQ and AC alloy specimens with maximum micro-hardness during non-isothermal processes also have the microstructure with coexistence of GPB zones and *S* phase (Fig. 5&6 (c) and (d)). Consequently, it could be concluded that the maximum mechanical properties should be associated with coexistence of GPB zones and *S* phases. Such phenomenon is associated with the thermal-stable Al_3Zr/Al_3Sc particles which normally distribute homogeneously and act as preferential sites for precipitation [24,47-52]. Early work proposed that Al_3Zr/Al_3Sc particles can effectively prevent vacancy condensation into dislocation loops during quenching after solution treatment, thus severely restricting heterogeneous nucleation of *S* phases in dilute Al-Cu-Mg alloys during artificial ageing [47]. Similar results were also reported in a later work in which Al_3Zr/Al_3Sc particles were found to make the *S* phase more homogeneously [48]. Recently, Han et. al. found that a highly dense GPB zones without requiring long-range diffusion for their formation were observed to dominate the precipitate microstructure due to the insufficient vacancies and dragging effect of Sc to Cu in an Al-Cu-Mg-Sc alloy [24]. For the present Al-Cu-Mg-Zr alloy, Zr addition can be thought to have the same influence on the formation of GPB zones and *S* phase. However, some works found that slower cooling rate would result in inhomogeneous distribution of Al_3Zr/Al_3Sc dispersoids, causing inhomogeneous nucleation of precipitates [49,50]. As a result, in WQ alloy with high cooling rate after heat treatment, highly dense and homogeneous GPB zones were observed at lower temperature or shorter holding time in this work, and homogeneous *S* phase at higher temperature or longer holding time, as

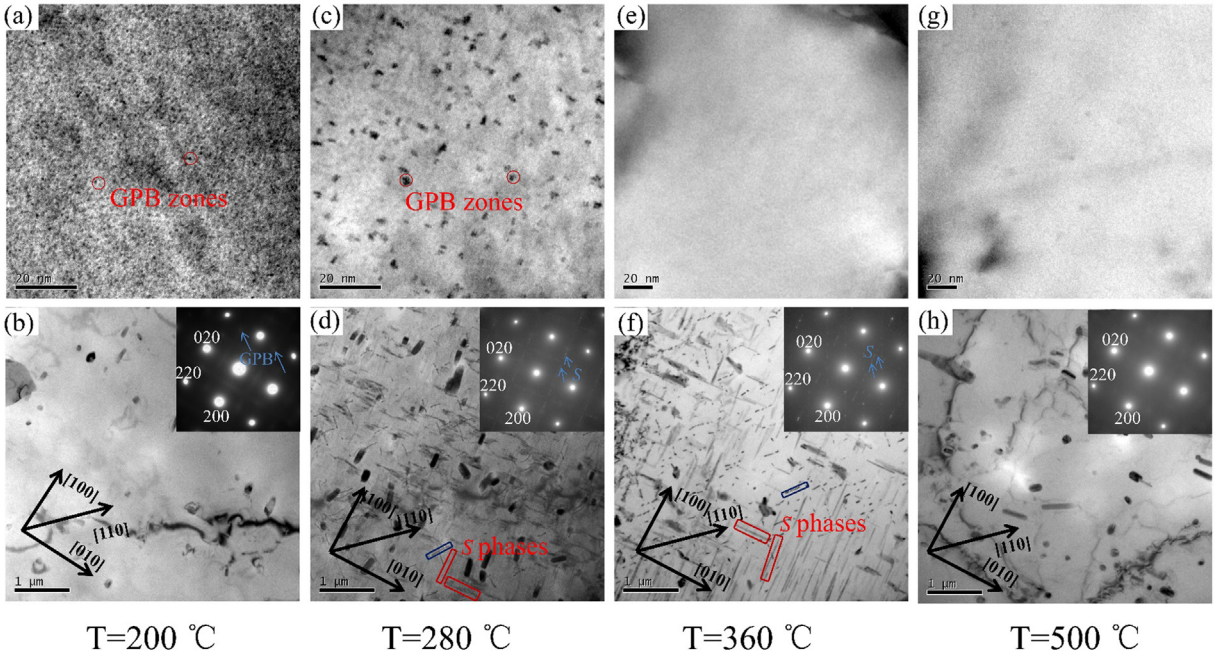

Fig. 5. TEM micrographs ($\langle 001\rangle_{Al}$ zone axis) of selected WQ alloy specimens during continuous heating process (2 °C/min): (a) & (b) 200 °C; (c) & (d) 280 °C; (e) & (f) 360 °C; (g) & (h) 500 °C.

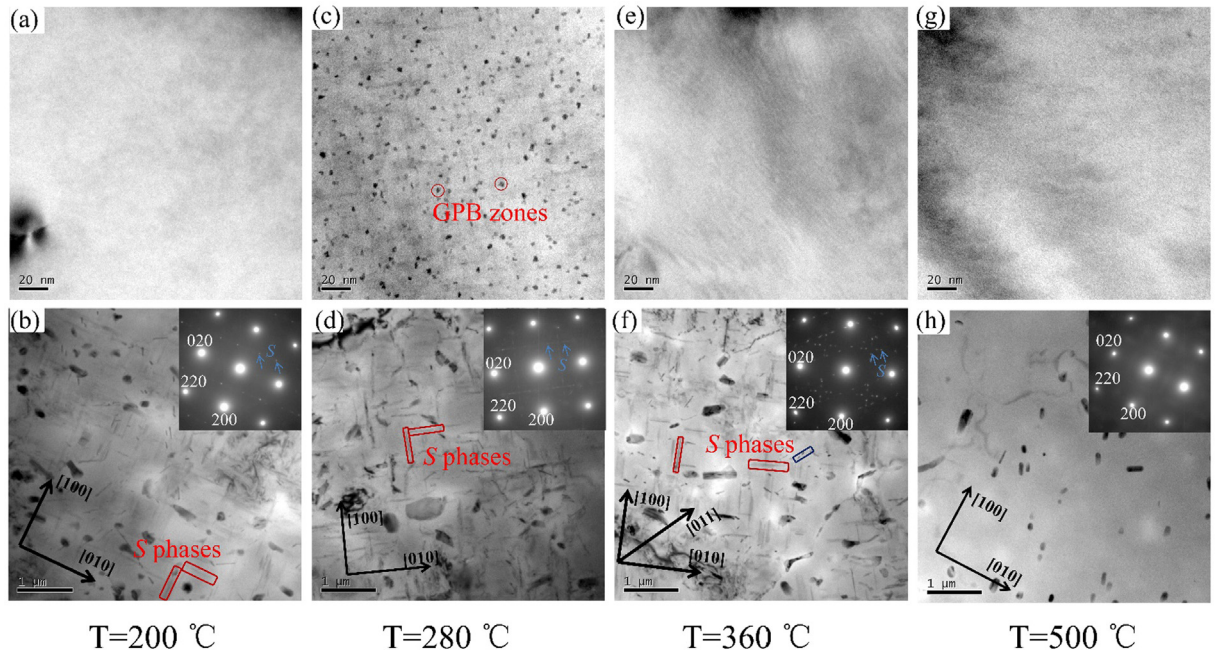

Fig. 6. TEM micrographs ($\langle 001\rangle_{Al}$ zone axis) of selected quenched AC alloy sample during continuous heating process (2 °C/min): (a) & (b) 200 °C; (c) & (d) 280 °C; (e) & (f) 360 °C; (g) & (h) 500 °C.

shown Figs. 5-7. Such precipitation microstructure contributed to the higher strength of WQ alloy. On the other hand, it is also reported recently that Zr/Sc addition would segregate at the interfaces of θ (Al_2Cu) phase during long-time holding at higher temperature, improving the thermal stability of θ (Al_2Cu) phase by inhibiting precipitates coarsening [51,52]. Consequently, in AC and FC alloy, the θ (Al_2Cu) phase formed during cooling are believed to be more stable. As a result, the initial dissolution temperature during non-isothermal heating process for AC and FC alloy is higher than WQ alloy, as shown in Fig. 3.

In addition, the morphology and orientation between *S* phase and Al matrix are also important for mechanical properties. In this scope, *S* phase has been reported to precipitate in the form of laths or rod-like shape with the $\{120\}_{Al}$ habit planes elongated along $\langle 100\rangle_{Al}$ direction [4-8]. The orientation relationships between *S* phase and the Al matrix are $[100]_{Al}//[100]_S$, $[02\bar{1}]_{Al}//[010]_S$, $[012]_{Al}//[001]_S$, and thus 12 equivalent variants of *S* phase to orientation relationship exist [4-8]. In this work, the dark dots in the figure with higher magnification represent GPB zones, as labeled in above figures. On the other hand, the figures with lower

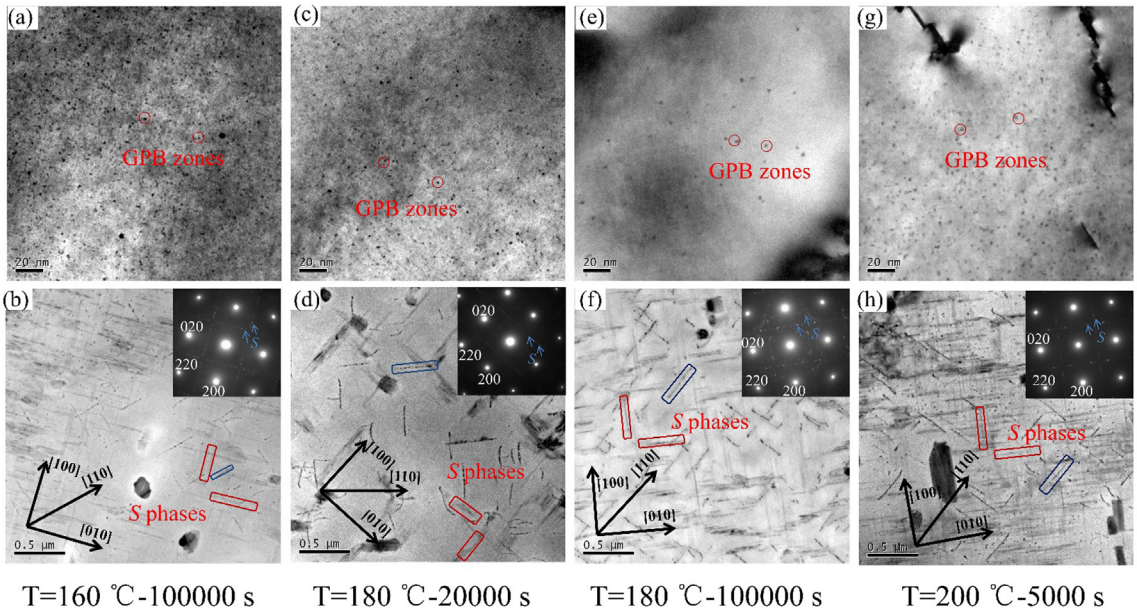

Fig. 7. TEM micrographs ($\langle 001\rangle_{Al}$ zone axis) of selected WQ alloy specimens under isothermal conditions: (a) & (b) 160 °C for 10^5 s; (c) & (d) 180 °C for 20000 s; (e) & (f) 180 °C for 10^5 s; (g) & (h) 200 °C for 10^5 s.

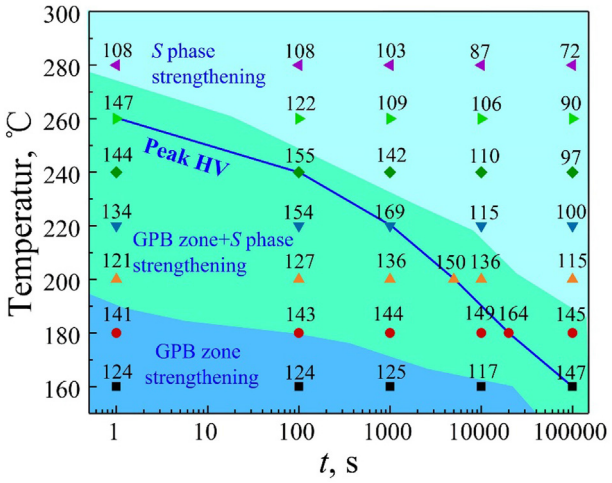

Fig. 8. The time–temperature-microstructure-properties map for Al-Cu-Mg-Zr alloy: different color zones represent different major strengthening phases.

magnification show the presence of two types of precipitates. The first type has relatively weak contrast and is marked in red rectangle, and the corresponding SAED patterns along the $[100]_{Al}$ zone axis are consistent with $\langle 100\rangle_S$, $\langle 021\rangle_S$ and $\langle 013\rangle_S$ variants of *S* phase in Al matrix [4-8]. Moreover, these fainter rods are perpendicular to each other and the rods edges are oriented along $\langle 100\rangle_{Al}$. The second type, which has rather strong contrast and is marked in blue rectangle in the figures, looks like that such points are connected along the $\langle 110\rangle_{Al}$ direction into a line. However, with increasing magnification of TEM images, the nature of this type of precipitates is revealed to be that many fine precipitates are arranged along the $\langle 110\rangle_{Al}$ direction, as shown in Fig. 9 (a)-(d). According previous works [4-8,22,39,40], the fine precipitates should be considered as the cross-sections of rod-like *S* phase. Therefore, the morphology features of *S* phase in the studied alloy should be recognized as rod-like, having habit planes of $\{110\}_{Al}$ and growth direction of $\langle 100\rangle_{Al}$. A schematic 3D drawing of the mixture of various *S* phases in Al matrix and its projection along $\langle 100\rangle_{Al}$ are shown in Fig. 9 (e) and (f).

4. Modeling

4.1. Modeling of electrical resistivity

In general, the electrical resistivity of metal gives a single value representing the average conduction electron scattering effects over all directions, which is highly dependent on temperature and the microstructures of metallic materials. As to Al alloys, their electrical resistivity is mainly governed by the electrical resistivity of pure Al ($\rho_{Al}(T)$), secondary precipitates (ρ_{ppt}) and alloying atoms dissolving in Al matrix (ρ_{solute}). $\rho_{Al}(T)$ is strongly temperature-dependent, but ρ_{ppt} and ρ_{solute} are thought to be temperature-independent [43-46]. In most cases, ρ_{ppt} is proportional to particle spacing (L) [43-46]: ($\rho_{ppt} \propto L^{-\frac{1}{2}}$), so it only shows a small increase for precipitates with a critical precipitate size ($1 \sim 2$ nm) and high density [43-46]. Therefore, the slight effect of precipitates and undissolved particles could be ignored because of much larger size and spacing of precipitates in the present alloy, as shown in previous TEM micrographs. Moreover, ρ_{solute} could be recognized as the summation of resistivity contributions from various solute atoms. Consequently, in the absence of strain (dislocation), the timely measured electrical resistivity of Al-Cu-Mg-Zr alloy at given temperature ($\rho(T)$) could be expressed in a general form based on Matthiessen's rule [43-46]:

$$\rho(T) = \rho_{Al}(T) + \rho_{solute} = \rho_{Al}(T) + \rho_0 + \sum\nolimits_i \rho_i C_{m,i} \quad (2)$$

where ρ_0 is the electrical resistivity of the studied alloy after completed precipitation, ρ_i and $C_{m,i}$ are the specific resistivity and the concentration of solute i in Al matrix, respectively [43-46]. In practice, the diffusion of elements Mn, Zr, Fe, and Si during aging is too slow to cause any significant change in electrical resistivity during precipitation. Hence, Eq. (2) could be written as:

$$\rho(T) = \rho_{Al}(T) + \rho_0 + \rho_{Cu} \cdot C_{m,Cu} + \rho_{Mg} C_{m,Mg} \quad (3)$$

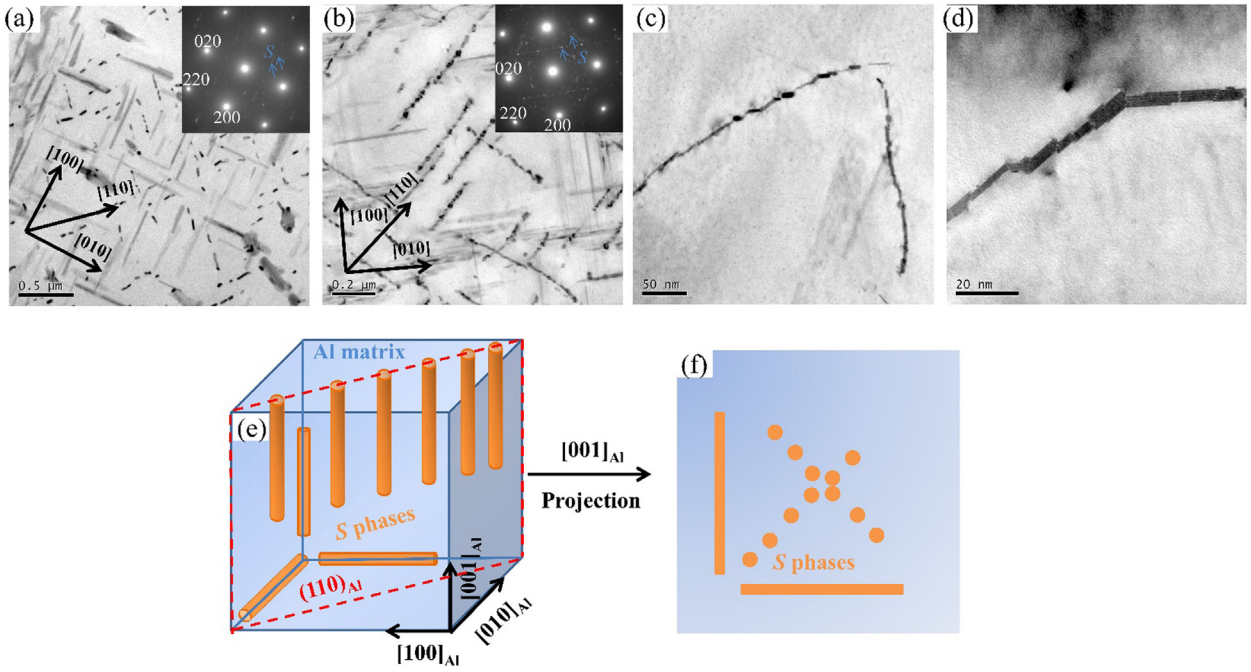

Fig. 9. (a)-(d) different magnifications of *S*-Al_2CuMg phase; (e) a schematic 3D drawing of *S*-Al_2CuMg phase in Al matrix and (f) the corresponding projection along $[001]_{Al}$.

As a result, the electrical resistivity and the concentration of alloying elements Cu an Mg in Al matrix can be deduced from each other. Detailed instructions on modeling of $\rho(T)$ by calculating $C_{m,Cu}$ and $C_{m,Mg}$ during precipitation process for the present alloy can refer to the Supplementary Information. In this study, the *in situ* $\rho(T)$ were used to obtain alloying elements concentration.

4.2. Modeling of precipitation and strength evolution

4.2.1. Fundamental framework of main strengthening contributions

Generally, various obstacle-strengthening contributions which dominate the yield strength will be considered: the intrinsic strength of Al matrix (σ_0), the grain boundary strengthening (σ_{GB}), the contribution due to forest dislocation (σ_d), the precipitation hardening contribution (σ_p), the solid solution contribution (σ_s). In the present alloy, σ_0 could be approximately equal to 10 MPa, and the dislocation could be considered to be almost absent due to lack of deformation and the grain size effect (σ_{GB}) is negligible [33,38]. Therefore, the yield strength (σ_y) can generally be expressed as:

$$\sigma_y = \sigma_0 + \sigma_p + \sigma_s \tag{4}$$

In addition, the conversion from yield strength to hardness can be done by the following equation:

$$HV = 0.33\sigma_y + 20 \tag{5}$$

4.2.2. Precipitation kinetics model

The precipitation strengthening effect (σ_p) is generally related to the relevant microstructural variables, including the volume fraction, size and number density of precipitates. Therefore, many precipitation kinetics models have been developed to obtain these microstructural variables. In the works of Esmaeili et al. [33,36,37], the relative volume fraction of precipitates (f_r) in JMAK model were obtained using experimental data from isothermal calorimetry and differential scanning calorimetry (DSC). And then a yield strength model in which the f_r was the main input data was successfully developed to predict the yield strength of Al-Mg-Si-Cu alloys during isothermal and non-isothermal aging. However, their work failed to obtain the real volume fraction of precipitates and to predict the precipitation kinetics during over ageing stage (coarsening of precipitates). Meanwhile, DSC tests involved different experimental errors, such as sample preparation and baseline correction [53]. In addition, the yield strengths obtained by their model were highly dependent on the relative volume fraction of precipitates (f_r) and independent on the size and density (spacing) of precipitate. On the other hand, the Kampmann and Wagner type numerical model (KWN model) was able to predict complete precipitation kinetics from nucleation to coarsening stages [38-41], and hence was used in this work. However, the evaluation of nucleation rate of precipitates was not introduced in this work, because nucleation is not expected to occur in the pre-precipitated AC and FC alloys, or when it does occur in WQ alloy it is expected to be less significant and to take place during preheating before holding [31,50]. Therefore, only growth and coarsening of precipitates are considered and evaluated by:

$$\frac{dr}{dt} = \frac{C_m - C_i}{C_p - C_i}\frac{D}{r} \tag{6}$$

where r is the radius of precipitates at time t, C_m represents the mean solute concentration in Al matrix (at.%), C_i stands for the solute concentration at the particle/matrix interface (at.%), C_p corresponds to the solute concentration in precipitate (at.%) and D is the diffusion coefficient of solute in Al matrix.

This model is generally considered valid for binary alloys and not strictly applicable for multicomponent alloys [38-41]. However, the atomic concentrations of Cu and Mg is close to 1 in the supersaturated solid solution of the present alloy (Table 1) and would remain nearly equal during precipitation processes, because the depletion of solutes from solution occurs in atomic proportion to the composition of precipitate (the Cu:Mg ratio is ~ 1 for both GPB zones and *S* phase). Therefore, the present alloy could be assumed to be pseudo-binary and hence C_p (Cu and Mg concentration in GPB zones and *S* phase) could be taken as 0.25 [35,39,40]. Moreover, the growth and coarsening of precipitates could also be assumed to be controlled by the diffusion of the slowest diffus-

ing element (Cu in this case) to the precipitate/matrix interface [35,39,40]. The diffusion coefficient of Cu (D_{cu}) could be expressed as:

$$D_{cu} = D_0 exp(-\frac{Q_{Cu}}{RT}) \tag{7}$$

where D_0 (1×10^{-5} m^2/s [54]) is the pre-exponential factor and Q_{Cu} (143 KJ/mol [54]) is the activation energy barrier, R and T are the gas constant and absolute temperature, respectively.

In the case of a diffusion-controlled process, C_i can be approximated by the equilibrium solute fraction in Al matrix in the presence of a particle of radius r at given temperature [35,39,40]:

$$C_i = C_e exp(\frac{2\gamma V}{rRT}) \tag{8}$$

where γ ($\gamma = 0.1206 + 2.186^{*}10^{-10} T^3$ (J/m^2) [39,40]) is the interfacial energy, V is the molar volume of precipitates (4×10^{-5} m^3/mol for S phase [31,32]), C_e is the equilibrium solute concentration which could be calculated using the regular solution model [39,40,50]:

$$C_{e,Cu} \cdot C_{e,Mg} = k \cdot [exp(-\frac{\Delta H}{RT})] \tag{9}$$

where k is a constant (600) and ΔH is the formation enthalpy of precipitates (75 KJ/mol [26,39,40]). Due to the Cu:Mg ratio of 1 during entire heat treatment, Eq. (9) could be further written as:

$$C_{e,Cu} = C_{e,Mg} = (k \cdot [\exp(-\frac{\Delta H}{RT})])^{0.5} \tag{10}$$

After getting the parameters in Eq. (5), the next step is to obtain the relationship between r and T or t. During non-isothermal process, temperature T is also function of time t. In addition, the precipitation process of GPB zones and S phase in the KWN model are evaluated in terms of a number of discreet small time steps during which new precipitates may nucleate and existing precipitates either grow or shrink. Then the precipitate size distribution and remaining solute concentration in matrix are re-calculated and used for the next time step as distinct groups [39,40,50]. Therefore, the integration of Eq. (6) could be expressed as:

$$r_{n+1} = 2^{1/2}\left[\frac{(C_m - C_i)Dt}{25 - C_i}\right]^{1/2} + r_n \,(C_m > C_i) \tag{11}$$

In addition, two main advantages of the KWN model are that growth and dissolution can be treated with the same kinetic equation and that coarsening arises naturally, as the interaction between small and coarse particles is considered through the matrix concentration balance. According to the published works [33,46], however, the dissolution kinetics from Eq. (11) in this work should be corrected as:

$$r_{n+1} = r_n - \frac{2(C_i - C_m)}{(25 - C_i)\pi^{1/2}}(Dt)^{1/2} \,(C_m < C_i) \tag{12}$$

4.2.3. Precipitation strengthening model

Different precipitation strengthening models were proposed based on the interaction of precipitates (both shearable and non-shearable) with dislocations [24,29,49,50]. In the present alloy, the GPB zones strengthening can be described well by modulus strengthening mechanism [38-40]:

$$\sigma_{GPB} = \frac{\Delta\mu}{4\sqrt{2}\pi}(f_{GPB})^{\frac{1}{2}} \tag{13}$$

where f_{GPB} is the volume fraction of GPB zones and $\Delta\mu$ is the difference in the shear modulus of Al matrix and GPB zones, which could be adjusted to fit the predicted strength to experimental results and has a value equal to 4.03 GPa [26,39,40].

According to above TEM characterizations, S-Al_2CuMg phase is approximately rod shaped with large size, thus mostly being considered to be non-shearable. Hence, S phase strengthening could be based on the Orowan looping mechanism [26,39,40]:

$$\sigma_S = \frac{0.112\mu b}{d_r} ln(\frac{1.136 d_r}{r_0})(f_s^{\frac{1}{2}} + 0.94 f_s + f_s^{\frac{3}{2}}) \tag{14}$$

where μ is shear modulus of Al matrix, d_r, L_r and f_s are diameter, length and volume fraction of rod-shaped S phase, respectively; b is the magnitude of Burgers vector (b = 2.86×10^{-10} m) and r_o is the inner cutoff radius for calculation of dislocation line tension, which is generally considered equal to b. Detailed instruction to get Eq. (14) can refer to the Supplementary Information.

4.2.4. Solid solution strengthening model

Further, the solid solution strengthening (σ_s) is determined by [26,33,36-41]:

$$\sigma_{ss} = k_{ss}(C_{m,i})^m \tag{15}$$

where k_{ss} is a constant calculated on the basis of data on strength of binary (Al-Mg and Al-Cu) dilute solid solutions, and m is a constant that has been taken in the past as either 2/3 or 1.

4.3. The integrated model and its implementation

4.3.1. Integrating the electrical resistivity and strength models

As described above, the common parameter in electrical resistivity, precipitation kinetics and strength models is the mean solute concentration in Al matrix (C_m) which is variational at different holding temperature and/or time during thermal processes. Therefore, an integrated model, which could predict the strength evolution by substituting the electrical resistivity into the precipitation and solution strengthening model, is given as:

$$\begin{cases} \sum_i \rho_i \cdot C_{m,i}(T,t) = \rho(T,t) - \rho_{Al}(T,t) \\ \frac{dr}{dt} = \frac{C_m - C_i}{C_p - C_i}\frac{D}{r} \\ \sigma_{ss} = k_{ss}(C_{m,i}(T,t))^m \end{cases} \tag{16}$$

4.3.2. Simplification of precipitation processes

The above precipitation kinetics and strength models are generally used for the strengthening contribution from single precipitate, so the precipitation processes involved two or more precipitates should be simplified theoretically. Therefore, because the dominant hardening phases in the present alloy include both GPB zones and S phases according to TEM micrographs, we simplified the precipitation processes by recognizing the ageing process of these two types of precipitates as two separate but continuous components. In other words, the GPB zones would assumed to be first formed at a lower temperature and/or shorter holding time, after which the S phase was formed soon. And the separated temperature or holding time could be determined according to $\Delta\rho$ evolution. Detailed explanation of such simplification can refer to the Supplementary Information.

4.3.3. Determination of modeling parameters

In the integrated model (Eq. (16)), it is difficult to determine the key parameter $C_{m,i}$. Although Khan et al [24,48] provided comprehensive approaches to predict precipitates size and related hardness for an Al-Cu-Mg alloy, the calculation procedure of $C_{m,i}$ in their KWN model was not given. In this study, because of the high sensitivity of *in situ* electrical resistivity to the solid solution con-

centration, the $C_{m,i}$ in matrix during heat treatment could be obtained continuously. Then the obtained data could be used to develop the KWN model, which is convenient. According to Eqs. (1)-(3) where the atomic concentration ratio of Cu and Mg is close to 1 during whole precipitation processes, the contribution from Cu and Mg atoms in the present alloy to the *in situ* electrical resistivity could be estimated by:

$$\Delta\rho = \rho_{Cu} \cdot C_{m,Cu} + \rho_{Mg} \cdot C_{m,Mg} + \rho_0 = C_{m,Cu} \cdot (\rho_{Cu} + \rho_{Mg}) + \rho_0 \quad (17)$$

Because ρ_0 is the electrical resistivity of the studied alloy after completed precipitation, it could be considered as the minimum $\Delta\rho$ of FC alloy (20 nΩ·m) in this study, as shown in Figs. 3 and 4. Therefore, the concentration of Cu and Mg atoms in Al matrix could be obtained by following equation:

$$C_{m,Cu} = C_{m,Mg} = \frac{\Delta\rho - \rho_0}{\rho_{Cu} + \rho_{Mg}} \quad (18)$$

According to previous works [46,50,54], ρ_{Cu} and ρ_{Mg} were taken as 8 and 5.3, respectively. For instance, the initial $\Delta\rho$ of WQ alloy, which represents the nearly complete dissolution of solute atoms in matrix, was about 42 nΩ·m. According to Eq. (18), the initial $C_{m,Cu}$ and $C_{m,Mg}$ in WQ alloy was then calculated to be about 1.65, which was comparable to the chemical composition in Table 1. Therefore, Eq. (18) could be considered as an effective approach to estimate $C_{m,Cu}$ and $C_{m,Mg}$. For other cases where $C_{m,Cu}$ and $C_{m,Mg}$ is not close to 1 but their initial composition and the composition of precipitates are known, detailed instruction to determine them can refer to the Supplementary Information.

According to Eq. (13) and (14), it is also critical to determine the volume fraction of GPB zones and *S* phase to obtain their strengthening contribution. A previous study was able to get the volume fraction of precipitates using electrical resistivity [50]. But one drawback is that electrical resistivity was measured after the equilibrium in the alloys was reached at several given temperatures, and the modeled volume fractions of precipitates were also under equilibrium status [50]. In this scope, *in situ* electrical resistivity could also provide effective approaches to evaluate the timely volume fraction of precipitates. According to published works [44-46], the *in situ* electrical resistivity of Al alloys can be expressed as follows:

$$\Delta\rho = \rho_0 + \sum_i \rho_i \cdot C_{m,i} = \rho_0 + \sum_i \rho_i \cdot (C_i^{sss} - f_v \cdot \frac{V_{ppt}}{V_{Al}} X_i^{ppt}) \quad (19)$$

where V_{ppt} (4×10^{-5} m^3/mol for *S* phases) and V_{Al} (1×10^{-5} m^3/mol) are the molar volume of precipitates and Al matrix respectively [31]; X_i^{ppt} is the atomic coefficient ratio of alloy element *i*

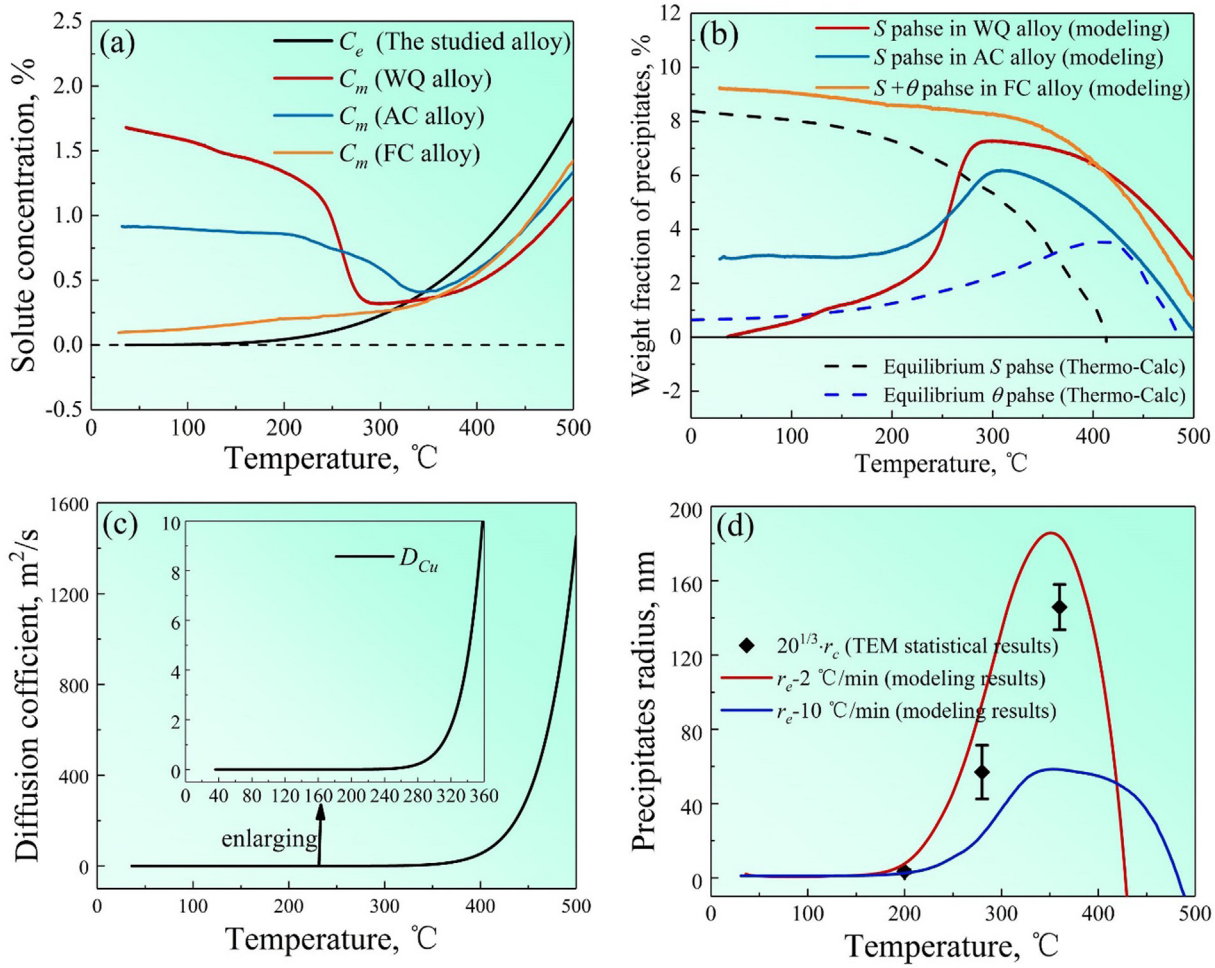

Fig. 10. Typical calculated parameters in the models: (a) Cu concentration in Al matrix, (b) weight fraction of precipitates, (c) diffusion coefficient of Cu atoms, (d) modeling and experimental radius of precipitates.

in precipitates and is equal to 0.25 in this study. Then, the volume fraction of precipitates could be calculated:

$$f_v = \frac{V_{ppt}}{V_{Al}} \frac{\sum_i \rho_i \cdot C_i^{sss} - \sum_i \rho_i \cdot C_{m,i}}{\sum_i \rho_i \cdot X_i^{ppt}} \tag{20}$$

where $\sum_i \rho_i \cdot C_i^{sss}$ and $\sum_i \rho_i \cdot C_{m,i}$ are *in situ* resistivity in supersaturated state and precipitation state, respectively. Meanwhile, if the molar mass of precipitate (m_{ppt}) and Al matrix (m_{Al}) are given, the mass fraction of precipitates can be expressed as:

$$f_w = \frac{m_{ppt}}{m_{Al}} \frac{\sum_i \rho_i \cdot C_i^{sss} - \sum_i \rho_i \cdot C_{m,i}}{\sum_i \rho_i \cdot X_i^{ppt}} \tag{21}$$

4.3.4. Modeling validation

As described above, the key input parameters in above model are the mean solute concentration in Al matrix ($C_{m,i}$, at.%) the volume fraction of precipitates (f_{v}) and the diffusion coefficient of Cu solute (D_{cu}). To verify the calculation expression of these parameters, typical calculated results are presented in Fig. 10. The equilibrium solute concentration (C_{e}) and the C_{m} of the three alloy specimens during non-isothermal processes with 2 °C/min are shown in Fig. 10 (a). Here C_{m} represent both the atomic concentrations of Cu and Mg ($C_{m,Cu} = C_{m,Mg}$), because their ratio would remain nearly 1 during the whole precipitation, as described in Eq. (6) and (18). The weight fraction evolutions of precipitates for the studied alloys during non-isothermal processes with 2 °C/min are presented in Fig. 10 (b). It is worthwhile to mention here that θ phase was predominant in FC ally but *S* phase in WQ and AC alloys according to thermodynamic calculations (Fig. 2). Hence different molar volume (5.4×10^{-5} m^3/mol for θ phase [31]) or mass fraction was used to calculated the volume and mass fraction evolutions of precipitates. The maximum mass fraction of precipitates for AC and WQ alloys are about 7.5% and that for FC alloy 9.2%, which are relatively consistent with thermodynamic calculations. D_{cu} is also present in Fig. 10 (c), which would be used to for thermodynamic and kinetic analysis in next section. In addition, the comparison between the modeled radius of precipitates (r) and quantitative statistics of TEM micrographs in WQ alloy are plotted in Fig. 10 (d). It is also important to mention here that the modeled r_e is the equivalent radius of spherical particle and the statistical radius (r_c) is the radius of cross-section of rod-shaped *S* phase [33]. And by adopting the aspect ratio ($l/2r_c$ = 10) [39,40], the relationship of $r_e^3 = 20r_c^3$ could be obtained. The comparison in Fig. 10 (d) shows a good agreement. Moreover, the decrease in modeled r_e to zero at about 430 °C indicates complete dissolution of *S* phase, which is also consistent with the thermodynamic calculation results. Therefore, the model approaches in this work are convincing and effective.

The modeled hardness during non-isothermal and isothermal processes are compared with experimental hardness values in Fig. 11. The data points with symbols represent measured hardness values, and the solid lines denote predicted hardness considering only GPB zones and *S* phase formed during thermal processes. Overall, there is a generally good agreement between modeled and experimental results for all temper alloys. In detail, the predictions during non-isothermal processes with a heating rate of 2 °C/min are highly in good agreement for the three temper alloys over the whole heating stage, as shown in Fig. 11 (a). With the heating rate increasing to 10 °C/min (Fig. 11 (b)), there are relatively big deviations between the modeling and experimental results for WQ and AC alloys at higher temperatures, although the prediction is still generally consistent with experimental values of FC alloy. For all isothermal processes, the variation trends of modeled results are similar with that of experimental results. However, the deviation between predicted results and measured results are with high values, especially at lower holding temperatures for WQ and AC alloys. All deviations would be explained and discussed in the next section.

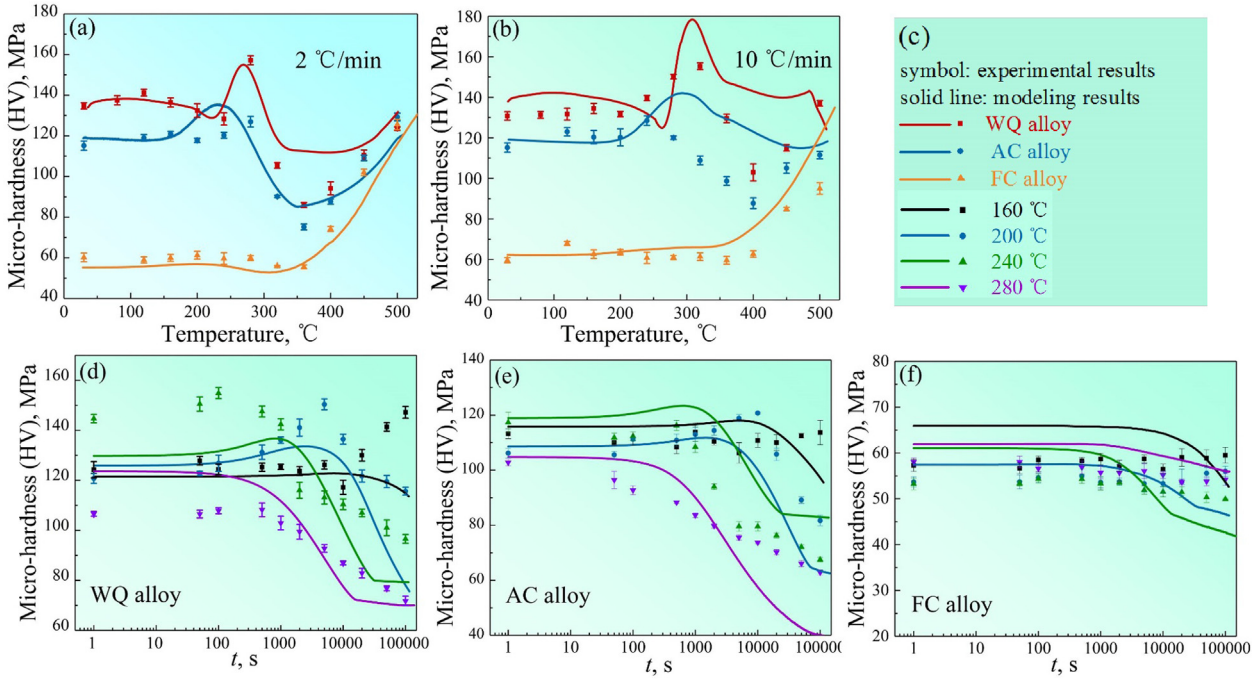

Fig. 11. Model predictions of hardness are compared with experimental results: continuous heating of (a) 2 °C/min (b) 10 °C/min; (c) legend illustration; isothermal holding for (c) WQ alloy (d) AC alloy and (e) FC alloy.

5. Discussions

It is known that the thermodynamic and kinetic origins for precipitation are the thermal activation energy and the thermodynamically unstable supersaturated solid solution after solution treatment. According to the KWN model, the equilibrium solute concentration (C_e) indicates the solid solubility in Al matrix after the studied alloy held at a given temperature for an infinite period of time to reach equilibrium. In other words, the mean solute concentration in Al matrix (C_m) is always trying to get to be closer to C_e. Therefore, the decomposition of supersaturated solid solution to form precipitates would occur when C_m is greater than C_e; otherwise, the precipitates would be re-dissolved [35]. Further, the magnitude of driving force to overcome nucleation and dissolution barriers is strongly related to different (C_m-C_e) or (C_e-C_m) [35]. However, it is widely accepted that the phase transformation in Al alloys is diffusion-controlled, and hence the precipitation and dissolution kinetics are also highly dependent on diffusion coefficient (D). According to Eq. (7) and Fig. 10 (c), the higher the temperature, the greater the value of diffusion coefficient (D), especially when the diffusion coefficient increases sharply above 400 °C. In the present work, the pre-precipitated microstructures of the studied alloy are affected by cooling conditions and preheating temperature. As shown in Fig. 1, most solid solutes are retained in Al matrix in WQ alloy because of few precipitates formation during fast cooling process. In AC alloy, a certain number of solid solutes still remained in Al matrix, although many solid solutes were consumed to form precipitates during air cooling. On the other hand, in FC alloy, the very slow cooling rate was able to allow the samples hold in the temperature range of 300–450 °C for a long time, resulting in the formation of massive coarse θ phases which were mainly formed at high temperature ranges due to the high diffusion abilities of various alloy elements. Therefore, the solid solutes in FC alloy have been almost consumed completely and very low supersaturated solid solubility is obtained, leading to stable status. Meanwhile, *in situ* electrical resistivity is an effective approach to reflect precipitation behavior in metallic materials owing to its high sensitivity to the concentration of impurities (or solid solution). As a result, the maximum initial $\Delta\rho$ is obtained in WQ alloy but the minimum $\Delta\rho$ in FC alloy after cooled from solution treatment in different ways. Consequently, the various pre-precipitation microstructures and different temperatures and/or holding time during thermal processes would both result in different precipitation behaviors of the studied alloy [44-46].

During non-isothermal processes of WQ alloy, as shown in Fig. 10 (a), the C_m is much bigger than C_e at the initial heating stage (30–240 °C), indicating that the thermodynamic conditions for precipitation are satisfied. However, the diffusion coefficient (D) in this temperature range is much low. As a result, only a limited number of precipitates formed and hence slight decrease in $\Delta\rho$ is observed. After that, rapid drop in $\Delta\rho$ to the minimum in the temperature range of 240–280 °C indicates fast formation of precipitation, which is attributed to big difference (C_m-C_e) and relatively high diffusion coefficient (D). With temperature increasing from 280 to 330 °C, the C_m is getting closely to C_e, so the driving force for precipitation becomes weak and the coarsening of precipitates is predominant. When C_e is greater than C_m, the dissolution of precipitates begins to occur. However, the difference (C_e-C_m) is not big enough in the temperature range of 330–360 °C, and therefore only fine precipitates could re-dissolve into Al matrix. Consequently, the integrated function of precipitation and dissolution behaviors in the temperature range of 280–360 °C are that the dissolution of small precipitates and the growth of large ones via a diffusive mass flow from shrinking to growing with virtually constant volume fraction. This process is the typical feature of "Ostwald ripening". In detail, the chemical composition and number of second phase particles could generally reach equilibrium in the later precipitation stage through nucleation and growth mechanisms. However, the dispersed distribution of fine precipitates enables the alloy to own high interfacial energy. To reduce the total interfacial energy, fine precipitates with high density tend to coarsen into the larger particles with smaller total interface energy and lower density distribution. Further, in the temperature range of 360–500 °C, the big difference (C_e-C_m) and much high diffusion coefficient (D) cause fast dissolution of precipitates, leading to rapid increase in $\Delta\rho$. On the other hand, the lower difference (C_m-C_e) in AC alloy than that in WQ alloy and low diffusion coefficient (D) at the initial heating stage (30–240 °C) could not provide enough driving force for precipitation. As a result, toughly unchanged $\Delta\rho$ is observed. After that, the thermodynamic and kinetic origins for precipitation in AC alloy are similar to that in WQ alloy. However, the coarsening behavior is not evident in AC alloy because the precipitates have grown to a certain large size before heating. For FC alloy, dissolution of small precipitates is predominant at the early heating stage (30–300 °C), after which C_m is lower than C_e in the temperature range of 300–500 °C. Therefore, diffusion coefficient (D) is the main factor to control the dissolution of precipitates. As a result, low diffusion coefficient (D) at lower temperatures and high diffusion coefficient (D) at higher temperatures result in the slow and fast increase in $\Delta\rho$, respectively, as shown in Fig. 3 (a). Moreover, the differences (C_e-C_m) in AC and FC alloys are bigger than that in WQ alloy during dissolution stage, leading to higher dissolution rate in Fig. 3 (b). Therefore, the precipitates in AC and FC alloys were re-dissolved more completely into Al matrix, resulting in higher $\Delta\rho$ at the end of heating (500 °C) than that in WQ alloy (Fig. 3 (a)). In addition, the influence of heating rate could be attributed to the time for diffusion of solid solutes. Although the difference (C_m-C_e) at 10 °C/min is higher than that at 2 °C/min during precipitation stage, the holding time at the same temperature ranges is shorter, resulting in relatively incomplete precipitation. As a result, both the value of minimum $\Delta\rho$ and the temperature to reach the minimum $\Delta\rho$ are higher at 10 °C/min than those at 2 °C/min. During dissolution stage, however, much higher diffusion coefficient (D) enables precipitates to be completely re-dissolved into Al matrix in relatively shorter time when the alloy heated at 10 °C/min.

During isothermal processes, the present alloy samples are preheated in furnace to target temperatures before isothermal holding stage, which is closer to industrial processes. In this case, the heating rate of specimens is generally fast at lower temperature ranges but become slow when the real-time temperature is close to target temperature. Therefore, it is a fact that the samples are held for a certain long time when the real-time temperature is getting close to target temperature and some precipitates have formed or re-dissolved during this stage. The influences of preheating stage on precipitation evolution ($\Delta\rho$) are shown in Fig. 12. For WQ alloy, C_m is always larger than C_e during both preheating and holding stage, so there would be continuous precipitation during both preheating and holding stage. Moreover, the higher the target temperature, the bigger the magnitude of the drop in $\Delta\rho$ during preheating stage, as shown in Fig. 12 (a). For instance, $\Delta\rho$ decreases from $\sim$ 42 nΩ·m to $\sim$ 23 nΩ·m during the process of preheating to 280 °C, indicating the formation of a large number of precipitates. As a result, C_m decreases significantly, leading to a decrease in the difference of (C_m-C_e) which provides driving force for precipitation. Therefore, the decreasing rate of $\Delta\rho$ (precipitation kinetics) in the process of holding at 280 °C is much lower than that at 200 °C and 240 °C (Fig. 4 (a)). This is also the reason that precipitation kinetics at 240 °C is slower than that 200 °C. For AC alloy, as discussed in non-isothermal processes, the initial

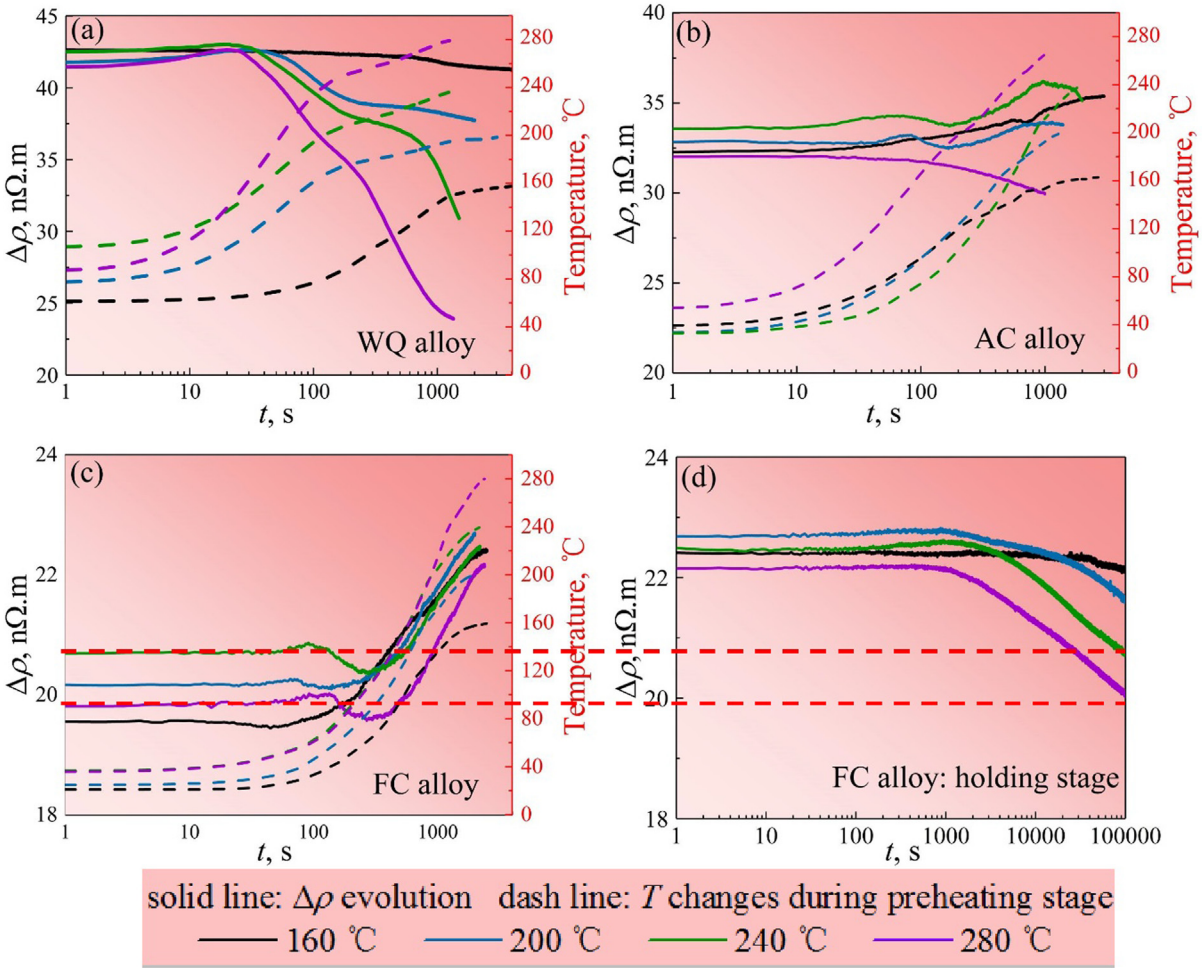

Fig. 12. $\Delta\rho$ evolution during the preheating stage of isothermal holding for (a) WQ alloy (b) AC alloy and (c) FC alloy and during holding stage for (d) FC alloy.

lower difference of (C_m-C_e), low diffusion coefficient (D) and limited preheating time could not provide enough driving force for precipitation in the processes of preheating with lower target holding temperature (160–240 °C). Therefore, as shown in Fig. 12 (b), $\Delta\rho$ increases slightly during preheating stages with target temperature of 160–240 °C. And these increases in $\Delta\rho$ could be attributed to that dissolution of the existing fine precipitates dominates during preheating stage with high heating rates [45,46]. However, subsequent holding stage could provide enough time for evident precipitation, although the lower driving force provided by the lower difference (C_m-C_e) and low diffusion coefficient (D) would result in low precipitation rates. By contrast, when increasing to higher holding temperature (e.g., 280 °C), the increased diffusion abilities lead to fast precipitation during preheating/holding stages, so there is continuous decrease in $\Delta\rho$ (Fig. 12 (b)). In FC alloy, as shown in Fig. 12 (c), the dissolution of precipitates is dominant during all preheating processes. However, the diffusion coefficient (D) is relatively low, leading to that there are only slight increases in $\Delta\rho$ (Fig. 12 (c)). After preheating stage, C_m becomes greater than C_e again, and hence precipitation is dominant during subsequent holding stage, resulting in decreases in $\Delta\rho$. In particular, $\Delta\rho$ decreases to the initial value after holding at 240 °C and 280 °C for 10^5 s, as plotted by the red dotted line. This indicates that the holding time is enough for the solid solutes, which were re-dissolved into Al matrix during the preheating stages, to completely precipitate out. However, at lower holding temperatures (160 °C and 200 °C), the relatively low diffusion coefficient (D) leads to incomplete decomposition of re-dissolved solid solutes.

Further, mechanical properties evolutions of Al alloys during non-isothermal and isothermal processes are generally the integrated response of microstructural evolutions. Therefore, precipitation behaviors under various heat treatment routes are significant. First of all, it is well known that the alloying elements dissolve into the Al matrix will significantly increase micro-hardness. On the one hand, precipitation can weaken solid solution strengthening. On the other hand, it will also strengthen the alloy by forming precipitates. According to strengthening model, the strengthening effect caused by precipitates is highly dependent on the size, density (particle spacing) and volume fraction of precipitates. In general, smaller size, higher density and higher volume fraction of precipitates will result in stronger precipitation strengthening. Therefore, WQ alloy owns the maximum value of initial micro-hardness due to the strong solid solution strengthening, but the minimum in FC alloy because of the large size and low density of precipitates. During non-isothermal processes, the first precipitates newly formed in WQ and AC alloys are GPB zones with nano-scale size, which only consume certain amount of solid solution atoms. There is still a large number of solid solution atoms present in WQ alloy. So the effect of solid solution strengthening is only slightly weakened. However, the size and density of fine GPB zones in WQ and AC alloys formed at the early heating stage is low, so precipitation strengthening is not strong enough. As a result, slight decrease in micro-hardness and toughly unchanged micro-hardness are observed in WQ and AC alloys in the temperature range of 30–240 °C, respectively. With the temperature increasing from 240 °C to 280 °C, the big difference of (C_m-C_e)

and relatively high diffusion coefficient (D) could accelerate the formation of S phase with high density in WQ and AC alloys. In addition, as mentioned in section *4.2*, S phase is considered to be non-shearable and hence has stronger strengthening contribution. Consequently, rapid increases in micro-hardness to peak value are both observed in WQ and AC alloys, although the effect of solid solution strengthening is significantly weakened. After that, the precipitates grow and coarsen with temperature increasing from 280 to 360 °C by the Ostwald ripening in which the average size of precipitates increases at the expense of small precipitates, resulting in decrease in the density of precipitates. Therefore, the micro-hardness of WQ and AC alloys decreases to the minimum, which are well predicted by the integrated model. However, because of the presence of some blocky θ phase formed in the temperatures ranges between 320 and 420 °C at the expense of S phase, which distributes irregularly and hence have weaker strengthening contribution, the predicted micro-hardness are slightly higher than the measured values for WQ and AC alloys, as shown in Fig. 11 (a). With the heating rate increasing to 10 °C/min (Fig. 11 (b)), the relatively bigger deviations are due to that a steady-state diffusion field is not established [36]. When θ phase is also re-dissolved into Al matrix, only solid solution strengthening is needed to be considered in the strength model, so the model can well predict micro-hardness again. For FC alloy, the dissolution of precipitates is always dominant during whole heating stage, so only the increment in solid solution strengthening should be considered. As a result, the predicted micro-hardness for FC alloy is highly in good agreement with experimental results. For all isothermal processes, the precipitation of GPB zones and S phase occurs simultaneously, as shown in Fig. 7. In this study, however, the KWN and strength models were established by recognizing the ageing process of these two types of precipitate ageing as two separate but continuous components, as mentioned in *section 4.3.2*. Moreover, different strengthening mechanisms and expressions account for precipitates with spherical, plate-like and rod-like morphology [39,40]. In this work, GPB zones are thought to be spherical and coherent with Al matrix and S phases are rod-like and incoherent, and their size distributed unevenly. Although we have converted Orowan looping strengthening mechanism of spherical precipitates to rod-like precipitates for S phases, the co-existence of GPB zones and S phases would interfere the real orientation with Al matrix, size distribution of both precipitates. As a result, the developed models fail to well predict micro-hardness evolution of the studied alloy, causing the high deviations between the predicted results and measured results during isothermal processes, especially at lower holding temperatures for WQ and AC alloys.

6. Conclusions

The precipitation evolutions of an Al-Cu-Mg-Zr alloy with various pre-precipitation microstructures (i.e., AC, WQ and FC alloy specimens) during non-isothermal and isothermal processes were unraveled by combining *in situ* electrical resistivity monitoring, hardness testing and TEM characterization. In addition, an integrated model coupling electrical resistivity, precipitation kinetics and strength evolution was established to rationalize the experimental observations. The following conclusions were drawn.

(1) Precipitation behaviors of Al-Cu-Mg-Zr alloy were highly dependent on pre-precipitation microstructures during both non-isothermal and isothermal processes, because the retained supersaturated solid solubility worked on the driving force for precipitation or dissolution significantly.

(2) During continuous heating, GPB zones and fine S phase were gradually formed at lower temperatures stages to strengthen the alloy. In higher temperature range, the dissolution of GPB zones, Ostwald coarsening of S phases and θ phase formation were observed and found to softening the alloy.

(3) During isothermal holding, precipitation behaviors of Al-Cu-Mg-Zr alloy were mainly the combined functions of annealing temperature and time. The incubation time for nucleation decreased with increasing temperature, and the Ostwald ripening occurred faster at higher temperatures or longer holding time. Preheating stages also had considerable influences on subsequent holding processes. A TTMP map was established to unravel precipitation characteristics and their strengthening functions.

(4) The *in situ* electrical resistivity was used as the main input data to develop an improved model on the basis of the classical KWN model. On the one hand, this integrated model could well predict the hardness evolutions of the studied alloy during non-isothermal and isothermal processes. On the other hand, it is revealed that the thermodynamic conditions for precipitation or dissolution is dominantly dependent on the difference of (C_m-C_e), and diffusion coefficient (D). The maximum hardness for heat-treated alloys is mainly attributed to the co-existence of GPB zones and S phase after verified by both experimental and modeling results.

Declaration of Competing Interest

The authors declare that they have no known competing financial interests or personal relationships that could have appeared to influence the work reported in this paper.

Acknowledgments

This work is supported by the National Natural Science Foundation of China (51874127, 51904099& 52075159), Hunan Provincial Innovation Foundation for Postgraduate (CX20190314), Graduate Training and Innovation Practice Base of Hunan Province and the Chinese Scholarship Council.

Data availability

There are no linked research data sets for this submission. The following reason is given:

The raw/processed data required to reproduce these findings cannot be shared at this time as the data also forms part of an ongoing study. Data will be made available on request.

Appendix A. Supplementary material

Supplementary data to this article can be found online at https://doi.org/10.1016/j.matdes.2022.110640.

References

[1] X.S. Zhang, Y.J. Chen, J.L. Hu, Recent advances in the development of aerospace materials, Prog. Aerosp. Sci. 97 (2018) 22–34, https://doi.org/10.1016/j.paerosci.2018.01.001.
[2] S.Y. Duan, L.K. Huang, S.H. Yang, Z. Zhou, S.J. Song, X.B. Yang, Y.Z. Chen, Y.J. Li, G. Liu, F. Liu, Uncovering the origin of enhanced strengthening in Li-added Al-Cu-Mg alloys, Mater. Sci. Eng. A 827 (2021) 142079, https://doi.org/10.1016/j.msea.2021.142079.
[3] L. Mei, X.P. Chen, C. Wang, J. Xie, Q. Liu, Good combination of strength and corrosion resistance in an Al-Cu-Mg alloy processed by a short-cycled thermomechanical treatment, Mater. Charact. 181 (2021) 111469, https://doi.org/10.1016/j.matchar.2021.111469.
[4] V.A. Esin, L. Briez, M. Sennour, A. Köster, E. Gratiot, J. Crépin, Precipitation-hardness map for Al-Cu-Mg alloy (AA2024-T3), J. Alloy Comp. 854 (2021) 157164, https://doi.org/10.1016/j.jallcom.2020.157164.
[5] Y. Liu, F. Teng, F.H. Cao, Z.X. Yin, Y. Jiang, S.B. Wang, P.K. Shen, Defective GP-zones and their evolution in an Al-Cu-Mg alloy during high-temperature aging,

J. Alloy Comp. 774 (2019) 988–996, https://doi.org/10.1016/j.jallcom.2018.10.061.
[6] InSu Kim, MinYoung Song, JaeHwang Kim, SungKil Hong, Effect of added Mg on the clustering and two-step aging behavior of Al-Cu alloys, Mater. Sci. Eng. A 798 (2020) 140123, https://doi.org/10.1016/j.msea.2020.140123.
[7] S.C. Wang, M.J. Starink, Precipitates and intermetallic phases in precipitation hardening Al-Cu-Mg-(Li) based alloys, Int. Mater. Rev. 50 (4) (2005) 193–215, https://doi.org/10.1179/174328005X14357.
[8] T.S. Parel, S.C. Wang, M.J. Starink, Hardening of an Al-Cu-Mg alloy containing Types I and II S phase precipitates, Mater. Des. 31 (2010) S2–S5, https://doi.org/10.1016/j.matdes.2009.12.048.
[9] X. Chen, C.D. Marioara, S.J. Andersen, J. Friis, A. Lervik, R. Holmestad, E. Kobayashi, Precipitation processes and structural evolutions of various GPB zones and two types of S phases in a cold-rolled Al-Mg-Cu alloy, Mater. Des. 199 (2021) 109425, https://doi.org/10.1016/j.matdes.2020.109425.
[10] L. Kovarik, M.J. Mills, Structural relationship between one-dimensional crystals of Guinier-Preston-Bagaryatsky zones in Al-Cu-Mg alloys, Scripta Mater. 64 (11) (2011) 999–1002, https://doi.org/10.1016/j.scriptamat.2011.01.033.
[11] L. Kovarik, S.A. Court, H.L. Fraser, M.J. Mills, GPB zones and composite GPB/GPBII zones in Al-Cu-Mg alloys, Acta Mater. 56 (17) (2008) 4804–4815, https://doi.org/10.1016/j.actamat.2008.05.042.
[12] C. Pan, Y. Yang, S. Wang, Y. Liu, S. Hu, Z. Wang, P. Shen, Atomistic building blocks of one-dimensional Guinier-Preston-Bagaryatsky zones in Al-Cu-Mg alloys, Mater. Des. 187 (2020) 108393, https://doi.org/10.1016/j.matdes.2019.108393.
[13] J.M. Silcock, The structural ageing charactcristics of Al-Cu-Mg alloys with copper: Magnesium weight ratios of 7:1 and 2.2:1, J. Inst. Met. 89 (1961) 203–210.
[14] S.B. Wang, Z.R. Liu, S.L. Xia, J. Key, J.H. Chen, Tetragonal-prism-like Guinier-Preston-Bagaryatsky zones in an AlCuMg alloy, Mater. Charact. 132 (2017) 139–144, https://doi.org/10.1016/j.matchar.2017.08.014.
[15] A. Deschamps, T.J. Bastow, F. de Geuser, A.J. Hill, C.R. Hutchinson, In situ evaluation of the microstructure evolution during rapid hardening of an Al-2.5Cu-1.5Mg (wt.%) alloy, Acta. Mater. 59 (8) (2011) 2918–2927, https://doi.org/10.1016/j.actamat.2011.01.027.
[16] J. Majimel, G. Molenat, F. Danoix, O. Thuillier, D. Blavette, G. Lapasset, M.-J. Casanove ¶, High-resolution transmission electron microscopy and tomographic atom probe studies of the hardening precipitation in an Al-Cu-Mg alloy, Philos. Mag. 84 (30) (2004) 3263–3280, https://doi.org/10.1080/14786430412331283983.
[17] L. Reich, S.P. Ringer, K. Hono, Origin of the initial rapid age hardening in an Al-1.7 at.% Mg-1.1 at.% Cu alloy, Philos. Mag. Lett. 79 (9) (1999) 639–648, https://doi.org/10.1080/095008399176689.
[18] G. Sha, R.K.W. Marceau, X. Gao, B.C. Muddle, S.P. Ringer, Nanostructure of aluminium alloy 2024: Segregation, clustering and precipitation processes, Acta Mater. 59 (4) (2011) 1659–1670.
[19] Y. Liu, X. Han, S. Wang, B.o. Wei, W. Li, Subtle atomistic processes of S-phase formation in Al-Cu-Mg alloys, J. Alloy Comp. 838 (2020) 155677, https://doi.org/10.1016/j.jallcom.2020.155677.
[20] X. Chen, D. Kim, M. O, C.D. Marioara, S.J. Andersen, A. Lervik, R. Holmestad, E. Kobayashi, Effect of pre-deformation on age-hardening behaviors in an Al-Mg-Cu alloy, Mater. Sci. Eng. A 820 820 (2021) 141557, https://doi.org/10.1016/j.msea.2021.141557.
[21] M. Gazizov, C.D. Marioara, J. Friis, S. Wenner, R. Holmestad, R. Kaibyshev, Precipitation behavior in an Al-Cu-Mg-Si alloy during ageing, Mater. Sci. Eng. A 767 (2019) 138369, https://doi.org/10.1016/j.msea.2019.138369.
[22] S.C. Wang, M.J. Starink, Two types of S phase precipitates in Al-Cu-Mg alloys, Acta Mater. 55 (3) (2007) 933–941, https://doi.org/10.1016/j.actamat.2006.09.015.
[23] F. Zhang, L.E. Levine, A.J. Allen, C.E. Campbell, A.A. Creuziger, N. Kazantseva, J. Ilavsky, In situ structural characterization of ageing kinetics in aluminum alloy 2024 across angstrom-to-micrometer length scales, Acta Mater. 111 (2016) 385–398.
[24] X. Han, S. Wang, B. Wei, S. Pan, G. Liao, W. Li, Y. Wei, Influence of Sc Addition on Precipitation Behavior and Properties of Al-Cu-Mg Alloy, Acta Metallurgica Sinica (English Letters) (2021) 1–13.
[25] M.J. Starink, S.C. Wang, The thermodynamics of and strengthening due to co-clusters: General theory and application to the case of Al-Cu-Mg alloys, Acta Mater. 57 (8) (2009) 2376–2389, https://doi.org/10.1016/j.actamat.2009.01.021.
[26] M.J. Starink *, N. Gao, L. Davin, J. Yan, A. Cerezo, Room temperature precipitation in quenched Al-Cu-Mg alloys: a model for the reaction kinetics and yield strength development, Philos. Mag. 85 (13) (2005) 1395–1417, https://doi.org/10.1080/14786430412331333374.
[27] M.J. Starink, N. Gao, J.L. Yan, The origins of room temperature hardening of Al-Cu-Mg alloys, Mater. Sci. Eng. A 387 (2004) 222–226, https://doi.org/10.1016/j.msea.2004.01.085.
[28] A.K. Gupta, P. Gaunt, M.C. Chaturvedi, The crystallography and morphology of the *S'*-phase precipitate in an Al(CuMg) alloy, Philos. Mag. A 55 (3) (1987) 375–387, https://doi.org/10.1080/01418618708209875.
[29] I.S. Zuiko, R. Kaibyshev, Ageing response of cold-rolled Al-Cu-Mg alloy, Mater. Sci. Eng. A 781 (2020) 139148, https://doi.org/10.1016/j.msea.2020.139148.
[30] Y.F. Cao, L.T. Jiang, D. Gong, G.Q. Chen, Z.Y. Xiu, Y.M. Cheng, X.F. Wang, G.H. Wu, Quantitative study of dimensional stability mechanism and microstructure evolution during precipitation process of 2024Al alloy, J. Mater. Sci. Techno. 90 (2021) 85–94, https://doi.org/10.1016/j.jmst.2021.04.002.
[31] G. Bo, F. Jiang, H. Su, L. Wu, J. Teng, D. Fu, H. Zhang, Static softening behavior and modeling of an Al-Cu-Mg-Zr alloy with various pre-precipitation microstructures during multistage hot deformation, Mater. Sci. Eng. A 778 (2020) 139094, https://doi.org/10.1016/j.msea.2020.139094.
[32] G.W. Bo, F.L. Jiang, Z.Y. Dong, G. Wang, H. Zhang, Revealing the influence of pre-precipitation microstructure on hot workability in an Al-Cu-Mg-Zr alloy, Mater. Sci. Eng. A 755 (2019) 147–157, https://doi.org/10.1016/j.msea.2019.04.009.
[33] S. Esmaeili, D. Lloyd, Modeling of precipitation hardening in pre-aged AlMgSi (Cu) alloys, Acta Mater. 53 (20) (2005) 5257–5271, https://doi.org/10.1016/j.actamat.2005.08.006.
[34] O.R. Myhr, Ø. Grong, H.G. Fjær, C.D. Marioara, Modelling of the microstructure and strength evolution in Al-Mg-Si alloys during multistage thermal processing, Acta Mater. 52 (17) (2004) 4997–5008, https://doi.org/10.1016/j.actamat.2004.07.002.
[35] M.J. Starink, S.C. Wang, A model for the yield strength of overaged Al-Zn-Mg-Cu alloys, Acta Mater. 51 (17) (2003) 5131–5150, https://doi.org/10.1016/S1359-6454(03)00363-X.
[36] S. Esmaeili, D.J. Lloyd, W.J. Poole, Modeling of precipitation hardening for the naturally aged Al-Mg-Si-Cu alloy AA6111, Acta Mater. 51 (12) (2003) 3467–3481.
[37] S. Esmaeili, D.J. Lloyd, W.J. Poole, A yield strength model for the Al-Mg-Si-Cu alloy AA6111, Acta Mater. 51 (8) (2003) 2243–2257, https://doi.org/10.1016/S1359-6454(03)00028-4.
[38] A. Deschamps, C.R. Hutchinson, Precipitation kinetics in metallic alloys: Experiments and modeling, Acta Mater. 220 (2021) 117338, https://doi.org/10.1016/j.actamat.2021.117338.
[39] I.N. Khan, M.J. Starink, Microstructure and strength modelling of Al-Cu-Mg alloys during non-isothermal treatments: Part 1-Controlled heating and cooling, Mater. Sci. Technol. 24 (12) (2008) 1403–1410, https://doi.org/10.1179/174328408X317020.
[40] I.N. Khan, M.J. Starink, J.L. Yan, A model for precipitation kinetics and strengthening in Al-Cu-Mg alloys, Mater. Sci. Eng. A 472 (1-2) (2008) 66–74, https://doi.org/10.1016/j.msea.2007.03.033.
[41] J. Miao, C. Zhang, A.D. Klarner, J. Zhang, E. Cinkilic, F. Zhang, A.A. Luo, Characterization and modeling of concurrent precipitation in Mg-Al-Sn alloys using an improved Kampmann-Wagner numerical (KWN) model, Materialia 21 (2022) 101348, https://doi.org/10.1016/j.mtla.2022.101348.
[42] D.F. Lam, C.C. Menzemer, T.S. Srivatsan, A study to evaluate and understand the response of aluminum alloy 2026 subjected to tensile deformation, Mater. Des. 31 (1) (2010) 166–175.
[43] B. Raeisinia, W.J. Poole, D.J. Lloyd, Examination of precipitation in the aluminum alloy AA6111 using electrical resistivity measurements, Mater. Sci. Eng. A 420 (1-2) (2006) 245–249, https://doi.org/10.1016/j.msea.2006.01.042.
[44] L. Tang, G. Bo, F. Jiang, S. Xu, J. Teng, D. Fu, H. Zhang, Unravelling the precipitation evolutions of AZ80 magnesium alloy during non-isothermal and isothermal processes, J. Mater. Sci. Technol. 75 (2021) 184–195, https://doi.org/10.1016/j.jmst.2020.10.040.
[45] F. Jiang, H.S. Zurob, G.R. Purdy, X. Wang, H. Zhang, Characterization of the isothermal precipitation kinetics of an Al-Zn-Mg-Cu alloy, Metall. Mater. Trans. A 49 (10) (2018) 5157–5168, https://doi.org/10.1007/s11661-018-4822-x.
[46] F.L. Jiang, H.S. Zurob, G.R. Purdy, H. Zhang, Characterizing precipitate evolution of an Al-Zn-Mg-Cu-based commercial alloy during artificial aging and non-isothermal heat treatments by in situ electrical resistivity monitoring, Mater. Charact. 117 (2016) 47–56, https://doi.org/10.1016/j.matchar.2016.04.014.
[47] S. Özbilen, H.M. Flower, Zirconium-vacancy binding and its influence on *S'*-precipitation in an Al-Cu-Mg alloy, Acta Metall. 37 (11) (1989) 2993–3000, https://doi.org/10.1016/0001-6160(89)90335-0.
[48] K. Yu, W. Li, S. Li, J. Zhao, Mechanical properties and microstructure of aluminum alloy 2618 with Al_3(Sc, Zr) phases, Mater. Sci. Eng. A 368 (1-2) (2004) 88–93, https://doi.org/10.1016/j.msea.2003.09.092.
[49] D. Godard, P. Archambault, E. Aeby-Gautier, G. Lapasset, Precipitation sequences during quenching of the AA 7010 alloy, Acta Mater. 50 (9) (2002) 2319–2329, https://doi.org/10.1016/S1359-6454(02)00063-0.
[50] M. Nicolas, A. Deschamps, Characterisation and modelling of precipitate evolution in an Al-Zn-Mg alloy during non-isothermal heat treatments, Acta Mater. 51 (20) (2003) 6077–6094, https://doi.org/10.1016/S1359-6454(03)00429-4.
[51] L. Jiang, B. Rouxel, T. Langan, T. Dorin, Coupled segregation mechanisms of Sc, Zr and Mn at θ' interfaces enhances the strength and thermal stability of Al-Cu alloys, Acta Mater. 206 (2021), https://doi.org/10.1016/j.actamat.2021.116634 116634.
[52] Y.H. Gao, C. Yang, J.Y. Zhang, L.F. Cao, G. Liu, J. Sun, E. Ma, Stabilizing nanoprecipitates in Al-Cu alloys for creep resistance at 300°C, Mater. Res. Lett. 7 (1) (2019) 18–25, https://doi.org/10.1080/21663831.2018.1546773.
[53] M.J. Starink, Analysis of aluminium based alloys by calorimetry: quantitative analysis of reactions and reaction kinetics, Int. Mater. Rev. 49 (2013) 191–226, https://doi.org/10.1002/chin.200504224.
[54] N.D. Alexopoulos, Z. Velonaki, C.I. Stergiou, S.K. Kourkoulis, Effect of ageing on precipitation kinetics, tensile and work hardening behavior of Al-Cu-Mg (2024) alloy, Mater. Sci. Eng., A 700 (2017) 457–467.